

Changes in arXiv version 2:

- Version 2 includes additional references and edits made prior to journal submission to correct typos and reduce the length.
- Motivated by queries about the sign of κ_{xy} , version 2 now includes additional calculations of the dependence of κ_{xy} on the in-plane orientation of the external magnetic field, which may be compared particularly with the experiments of Ref. [3,4]. Results of these calculations are depicted in section S10 of the supplemental material.
- During the additional calculations, we found two compensating errors in version 1, which could influence the computed sign of κ_{xy} . These have now been corrected. The first was that the orientation of the RuCl_6 octahedra depicted in the figures of the main text was mismatched with the structure employed in the first-principles calculations (depicted in Fig. 4 in the supplemental material). The difference was the orientation of the cubic axes relative to the cell axes. The relevant figures have now been updated to reflect this change. The second error was a missing minus sign in equation (101) in supplemental section S7. These errors compensated each other, such that the computed phonon Berry curvature and conclusion of $\kappa_{xy} > 0$ for $B \parallel a$ remains unchanged. The only consequence of correcting these errors is the reversal of the sign of $\eta_q^{\nu, \nu'}$, which is reflected in the updated Fig. 7 of the supplemental.

We are very thankful for the queries about the sign of κ_{xy} for prompting the discovery of these errors. None of the conclusions of version 1 were otherwise impacted.

- It may be noted that Ref. [3,4] report $\kappa_{xy} < 0$ for $B \parallel a$, while Ref. [9] reports $\kappa_{xy} > 0$ for $B \parallel a$. The differing signs in these experimental works arise from a different definition of crystallographic coordinates relative to the cubic (x, y, z) axes. Both experimental results are in agreement with each other, and correspond to the computed sign of κ_{xy}^{ph} obtained in this work.

Spin-Phonon Coupling in Transition Metal Insulators II: Spin-Orbital Moments, Chiral Phonons and Application to α -RuCl₃

Ramesh Dhakal,¹ David A. S. Kaib,² Sananda Biswas,² Roser Valentí,² and Stephen M. Winter^{1,*}

¹*Department of Physics and Center for Functional Materials, Wake Forest University, Winston-Salem, North Carolina 27109, USA*

²*Institute of Theoretical Physics, Goethe University Frankfurt, Max-von-Laue-Straße 1, 60438 Frankfurt am Main, Germany*

(Dated: August 15, 2024)

We apply a recently developed first-principles based approach for treating generic spin-phonon couplings in materials with strong spin-orbit coupling to study α -RuCl₃. Of particular focus is the potential for this material to exhibit a phonon thermal Hall effect induced by spin-phonon interactions. We find that spin-orbit coupling significantly enriches the form of these interactions, and imbues them with chirality that is conducive to generating finite phonon Berry curvatures. We show that this leads to a phonon thermal Hall effect that qualitatively reproduces the measured field dependence of κ_{xy} without requiring a field-induced spin liquid.

Reports of a large thermal Hall effect (THE) in α -RuCl₃[1–10], and a wide range of other magnetic insulators having spin-orbital-coupled local moments[11–21], has led to significant debate over the origin of this effect. The varying phenomenology of different materials points to possible contributions from different heat carriers. These may include magnetic excitations (spinons[1–4, 22–24] and topological magnons[9, 25–28]), as well as phonons, which experience weak Lorentz forces acting on charged ions[29–32], extrinsic disorder-induced skew-scattering[33–36], and/or intrinsic effects of spin-phonon coupling. The latter case includes the formation of topological magnon-polarons[37–43], effects of phenomenological “Raman” spin-phonon couplings[44–46], and more general effects of scattering from collective spin excitations[47–52]. Detailed analysis of the thermal Hall conductivity κ_{xy} has suggested that phonons likely play a non-negligible role in α -RuCl₃[6, 53], which is compatible with experimental evidence for strong magnetoelastic coupling[54–58]. However, part of the continuing ambiguity stems from a lack of detailed understanding of the form and magnitude of the spin-phonon couplings, and their consequences on thermal transport. Due to the importance of the THE in identifying topologically ordered ground states[22, 59–61], a complete understanding of phononic contributions is vital.

While the theory of spin-lattice coupling is well-developed[62–66], recent advancements in first principles methods[67–69] now make it possible to address these questions in material-specific studies. In this work, we employ the recently introduced (des Cloizeaux) effective Hamiltonian (dCEH) approach[69] to make a comprehensive analysis of spin-phonon couplings in α -RuCl₃, with a view to address the phonon THE. We conclude that “Raman” spin-phonon couplings play no role in this material. Instead, symmetry-enforced winding of the other spin-phonon couplings in momentum space induces a finite phonon Hall viscosity via the dissipationless scatter-

ing mechanism of [47, 48].

We consider the lowest-order spin-phonon couplings \mathcal{H}_{sp} for $j_{1/2}$ moments[69]:

$$\begin{aligned} \mathcal{H}_{\text{sp}} = & \sum_{q\nu,(ij)} u_{q\nu} \mathcal{A}_{(ij)}^{q\nu} + \sum_{q\nu,(i)} p_{q\nu} \mathcal{G}_{(i)}^{q\nu} \\ & + \sum_{q\nu q'\nu',(i)} u_{q\nu} p_{q'\nu'} \mathcal{L}_{(i)}^{q\nu; q'\nu'} \end{aligned} \quad (1)$$

where $u_{q\nu} = (a_{-q\nu}^\dagger + a_{q\nu})$ and $p_{q\nu} = i(a_{-q\nu}^\dagger - a_{q\nu})$, and $a_{q\nu}^\dagger$ creates a phonon with momentum q in band ν . The summation over (i) refers to the two unique Ru sites in a given honeycomb unit cell [Fig. 1(i)], and (ij) refers to the three unique nearest-neighbor bonds. The q -space spin and bond operators are:

$$\mathcal{A}_{(ij)}^{q\nu} = \frac{1}{\sqrt{N}} \sum_{\text{u.c.}}^N (\mathbf{S}_i \cdot \mathbb{A}_{(ij)}^{q\nu} \cdot \mathbf{S}_j) e^{-iq \cdot (r_i + r_j)/2} \quad (2)$$

$$\mathcal{L}_{(i)}^{q\nu; q'\nu'} = \frac{1}{N} \sum_{\text{u.c.}}^N (\mathbf{L}_{(i)}^{q\nu; q'\nu'} \cdot \mathbf{S}_i) e^{-i(q+q') \cdot r_i} \quad (3)$$

$$\mathcal{G}_{(i)}^{q\nu} = \frac{1}{\sqrt{N}} \sum_{\text{u.c.}}^N (\mathbf{G}_{(i)}^{q\nu} \cdot \mathbf{S}_i) e^{-iq \cdot r_i} \quad (4)$$

where u.c. refers to unit cells, and \mathbf{S}_i describe the $j_{1/2}$ moments. Contributions quadratic in u , which are associated with magnetostriction, have been omitted. The couplings \mathbb{A} are matrices, and represent the linear dependence of the intersite magnetic couplings on the atomic positions. The couplings \mathbf{G} and \mathbf{L} are vectors; these result from the dependence of the specific spin-orbital composition of the $j_{1/2}$ moments on the atomic positions[69].

To estimate the bare spin and spin-phonon couplings, we follow the dCEH approach of [69]. Full details are given in [70]. Briefly, we perform exact diagonalization of a coupled electron-phonon Hamiltonian on each site or bond of interest, and project the resulting low-energy

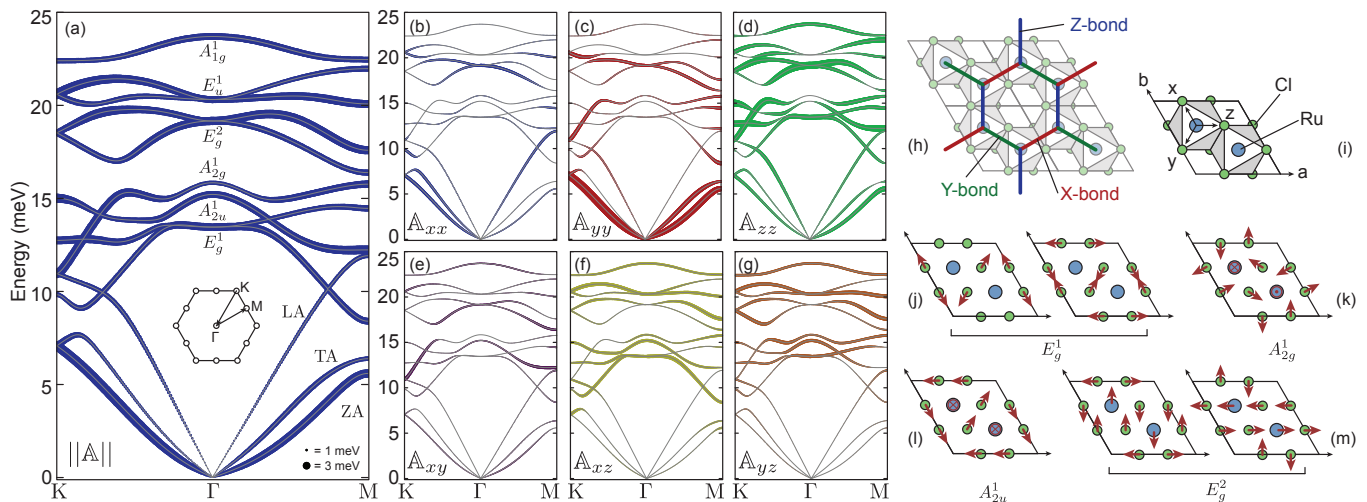


FIG. 1. Momentum dependence of the computed $\mathbb{A}_{(ij)}^{q\nu}$ spin-phonon couplings for the nearest-neighbor Z-bond along the high symmetry K- Γ -M path. (a): Frobenius norm $\|\mathbb{A}\|$. (b)-(g): Magnitude of different components of \mathbb{A} in cubic coordinates. (h): Four unit cells of α -RuCl₃ showing definition of nearest-neighbor X-, Y-, and Z-bonds. (i): Unit cell showing definition of cubic x, y, z coordinates. (j)-(m): Primary displacements associated with $q = 0$ optical phonons.

Hamiltonians onto ideal $j_{1/2}$ states with different numbers of phonon quanta. The inclusion of phonons explicitly as hard-core bosons allows for the extraction of generic spin-phonon couplings in addition to the usual spin-spin couplings. These results are combined with *ab-initio* phonon calculations to yield the full q, ν -dependent spin-phonon Hamiltonian.

To reduce the complexity of the computations, we utilize a relaxed and symmetrized $P\bar{3}1m$ structure with AA stacking of adjacent layers, which aids in the symmetry analysis below. In this structure, each Ru site has D_3 point group symmetry, and each nearest-neighbor bond has C_{2h} symmetry. For the symmetrized structure, with reference to the spin Hamiltonian $\mathcal{H}_s = \sum_{ij} \mathbf{S}_i \cdot \mathbb{J}_{ij} \cdot \mathbf{S}_j$, we compute the zeroth order spin couplings as $(J, K, \Gamma, \Gamma') = (-2.79, -5.96, +3.06, -0.12)$ meV, where:

$$\mathbb{J}_{\text{Z-bond}} = \begin{pmatrix} J & \Gamma & \Gamma' \\ \Gamma & J & \Gamma' \\ \Gamma' & \Gamma' & J + K \end{pmatrix} \quad (5)$$

for the nearest-neighbor Z-bonds [Fig. 1(h)]. The other bonds are related by symmetry [71, 72]. The computed couplings are sufficiently close to reported bulk values [72–80] to provide confidence in the computed spin-phonon couplings.

In Fig. 1, we show the computed phonon dispersions and $\mathbb{A}_{(ij)}^{q\nu}$ couplings for the nearest-neighbor Z-bond. The \mathbf{G} and \mathbf{L} couplings are found to be several orders of magnitude weaker, and are discussed in detail in [70]. Despite consideration of the artificial $P\bar{3}1m$ structure, the dispersion of the phonons for in-plane momenta reproduces experimental measurements relatively well [81–83]. From Fig. 1(b)-(g), one can see that the magnitude of the different components of the spin-phonon bond operators are

strongly momentum- and band-dependent. The specific coupling for each band can be rationalized from their real-space displacements, pictured in Fig 1(j)-(m). For example, the lowest optical mode at $q = 0$, labelled E_g^1 , primarily involves the symmetric motion of the Cl atoms bridging the nearest-neighbor bonds. For the Z-bond, this modulates the ligand-assisted hopping between d_{yz} and d_{xz} orbitals, which is the primary source of the Kitaev coupling K [71, 72]. As a consequence, \mathbb{A}_{zz} is the largest component of the spin-phonon coupling on the Z-bond, as shown in Fig. 1(d). The E_g^2 mode involves a similar in-plane motion of the Cl atoms, but also a modulation of the Ru positions along the bond direction. The latter motion affects the direct $d_{xy} - d_{xy}$ hopping, which alters the Γ and J couplings. For this reason, finite contributions to \mathbb{A}_{xx} and \mathbb{A}_{xy} are apparent. Full analysis of the $q = 0$ couplings is given in [70]. Here, we emphasize that the competing exchange processes in $j_{1/2}$ systems imply strongly anisotropic and band-dependent forms of the spin-phonon coupling.

The three acoustic modes, which are most relevant for low-temperature thermal transport, nominally correspond to out-of-plane motion transverse to the q -vector (labelled ZA), in-plane transverse motion (TA), and in-plane longitudinal motion (LA). Near $q = 0$, assuming linear dispersion of the acoustic phonons, the spin-phonon couplings scale as [70]:

$$\mathbb{A}_{(ij)}^{q\nu}|_{q \approx 0} = \mathbb{A}_{(ij)}^{\theta\nu} |q|^{1/2} \quad (6)$$

$$\mathbf{L}_{(i)}^{q\nu; -q\nu'}|_{q \approx 0} = \mathbf{L}_{(i)}^{\theta\nu, \nu'} |q|^2 \quad (7)$$

$$\mathbf{G}_{(i)}^{q\nu}|_{q \approx 0} = \mathbf{G}_{(i)}^{\theta\nu} |q|^{3/2} \quad (8)$$

where θ denotes the angle in q -space measured from the

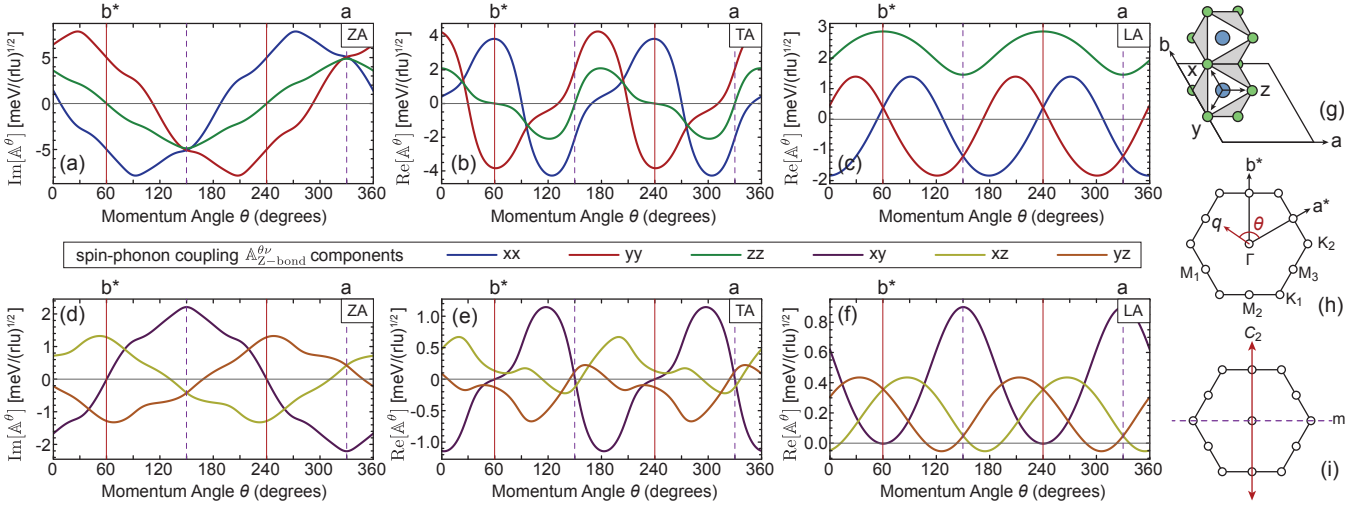


FIG. 2. Computed acoustic-mode spin-phonon couplings $\mathbb{A}_{ij}^{\theta\nu}$ for the nearest-neighbor Z-bond as a function of the momentum angle θ . (a)-(c): diagonal \mathbb{A}_{xx} , \mathbb{A}_{yy} , and \mathbb{A}_{zz} components. (d)-(e): off-diagonal \mathbb{A}_{xy} , \mathbb{A}_{xz} , and \mathbb{A}_{yz} components. The acoustic modes ZA, TA, and LA are labelled in the upper right of each panel. (g) Z-bond in real space showing definition of the unit cell a, b axes and cubic (x, y, z) coordinates. (h) first Brillouin zone showing definition of the a^*, b^* axes, and θ (measured from the a^* axis). (i) orientation, in q -space, of the relevant symmetry operations for the Z-bond.

a^* -axis [Fig. 2(h)]. These are complex quantities that satisfy $f(q) = f^*(-q)$. The spin-phonon Hamiltonian is invariant under simultaneous gauge transformations on the phonon operators and spin-phonon couplings[70]. We choose a gauge in which both are smooth everywhere in the 2D Brillouin zone except at $q = 0$. This requires, for example, the $q \rightarrow 0$ limit of \mathbb{A}_{ZA} to be completely imaginary, while \mathbb{A}_{TA} and \mathbb{A}_{LA} are completely real. This distinction reflects the fact that the direction of the real-space (in-plane) atomic motion of the LA and TA modes rotates with the momentum angle θ , while the ZA mode represents out-of-plane motion, independent of θ .

Fig. 2 shows the computed θ -dependence of the $\mathbb{A}_{ij}^{\theta\nu}$ matrices in cubic coordinates for the nearest-neighbor Z-bond. At each q -point, the combination of time-reversal and inversion ensures that \mathbb{A} is symmetric, i.e. $\mathbb{A}_{\alpha\beta} = \mathbb{A}_{\beta\alpha}$. In real space, the Z-bond is symmetric with respect to $C_2 \parallel b^*$ and $m \perp b^*$ [Fig. 2(i)]. This restricts the spin-phonon couplings for certain high-symmetry momenta. For $q \parallel b^*$ (parallel to the bond), the ZA and TA modes are odd with respect to the C_2 , while the LA modes are even. For $q \perp b^*$ (perpendicular to the bond), the TA modes are odd with respect to m , while the ZA and LA modes are even. Symmetry enforces some of the couplings to change sign when rotating around the origin of the Brillouin zone. For example, for the ZA mode: at $q \perp b^*$, $\mathbb{A}_{xx} = \mathbb{A}_{yy}$, while at $q \parallel b^*$, $\mathbb{A}_{xx} = -\mathbb{A}_{yy}$. Unless both couplings vanish at $q \parallel b^*$ (as would be the case with weak SOC), one must change sign an odd number of times when rotating between the two directions. The net result is that the spin-phonon couplings tend to wind around the origin of the Brillouin zone. Under relatively

generic conditions, this can lead to a finite phonon Berry curvature, as elaborated below.

We now consider the effects of the computed couplings on thermal transport. At fixed low temperature, the average in-plane longitudinal phonon thermal conductivity κ_{xx}^{ph} follows[70]:

$$\kappa_{xx}^{\text{ph}} \propto \sum_{\nu} \int_0^{2\pi} d\theta \tau_{\nu}^{\theta} \quad (9)$$

where the summation is over acoustic bands, τ_{ν}^{θ} is the band-dependent relative phonon lifetime, approximated by $\tau_{\nu}^{\theta} \propto \omega_{q\nu} / \text{Im}[\Pi_q^{\nu\nu}(\omega_{q\nu})]$, and $\Pi_q^{\nu\nu}$ is the phonon self-energy. The contribution from spin-phonon scattering, at one-loop order, is given by the dynamical bond-bond correlation[70]:

$$\Pi_q^{\nu\nu'}(i\omega_n) = - \left[\int_0^{\beta} d\tau e^{i\omega_n\tau} \langle \mathcal{A}_{q\nu}(\tau) \mathcal{A}_{-q\nu'}(0) \rangle \right] \quad (10)$$

To study the qualitative evolution of κ_{xx}^{ph} with in-plane magnetic field $B \parallel a$, we estimated the bond-bond correlations via exact diagonalization (ED) using the 24-site cluster depicted in Fig. 3(g). We employ a bare spin Hamiltonian \mathcal{H}_s including the nearest-neighbor couplings computed for the relaxed structure [Eq. (5)], plus a third-neighbor $J_3 = +0.8$ meV, and an in-plane g -value of $g_{ab} = 2.3$. These fall into the range of reported values in the literature[80]. Since ED does not provide a fine q -dependence, we retain the q -dependence of the spin-phonon operators, but approximate the low- q bond correlations with their $q = 0$ values. To compute κ_{xx} , the discrete poles of $\Pi_q^{\nu\nu}(\omega)$ were Lorentzian broadened with

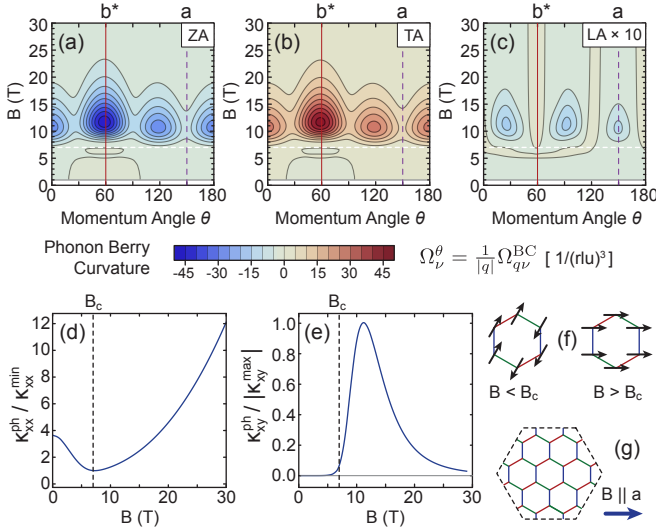


FIG. 3. Phonon thermal transport quantities for $B||a$. (a)-(c): Berry curvature $\Omega_{q\nu}^{BC}/|q|$. (d): Average in-plane longitudinal thermal conductivity $\kappa_{xx}^{ph}/\kappa_{xx}^{\min}$. (e): Thermal Hall conductivity $\kappa_{xy}^{ph}/|\kappa_{xy}^{\max}|$. (f) zigzag ($B < B_c$) and polarized ($B > B_c$) magnetic states. (g) 24-site cluster employed in ED calculations of the bond correlations. In (a)-(c), $B_c = 7$ T is indicated by a horizontal dashed white line.

a width of $\gamma = 0.5$ meV to extrapolate to low frequency. This produces an unavoidable dependence of the computed self-energy on γ . For this reason, we plot κ_{xx}^{ph} relative to its minimum value (at $B = 7$ T) in Fig. 3(d), which is insensitive to γ [70].

For $B||a$, the spin model has two phases [Fig. 3(f)]. For $B < B_c \approx 7$ T, it is nominally in an antiferromagnetic zigzag phase; for $B > B_c$ it adopts an asymptotically polarized phase. As shown in Fig. 3(d), the computed average in-plane κ_{xx}^{ph} reaches a minimum near the critical field. This behavior is consistent with experimental measurements[2, 3, 54, 84, 85], which report reduction of κ_{xx} at B_c by factors of 2 - 5 compared to the zero-field value. This can be simply understood. At both low field and high field, the spin excitations are gapped and well separated in energy from the low- q acoustic phonons. At the critical field, the closure of the spin gap implies an increased density of low-energy spin excitations, which enhances scattering. Since $\Pi_q^{\nu\nu}$ is a dynamical bond-bond correlation, the closure of a one-magnon gap at any q -point enhances scattering for phonons near $q = 0$ due to contributions from multi-magnons at low- q . ED does not capture a complete gap-closing due to finite size effects, likely resulting in a broader minimum in $\kappa_{xx}(B)$ than found in experiments.

Due to spin-phonon coupling, the phonons can also acquire a finite Hall viscosity $\eta_q^{\nu\nu}$, which leads to an anomalous velocity contribution to κ_{xy}^{ph} . In the off-shell one-loop

approximation[47, 48]:

$$|q|^2 \eta_q^{\nu\nu'} = 2 \sum_{(i)} \langle \mathcal{L}_{(i)}^{-q\nu'; q\nu'} \rangle + \lim_{i\omega_n \rightarrow i0} \frac{2i \sqrt{\omega_{q\nu} \omega_{q\nu'}}}{i\omega_n} \Pi_q^{\nu\nu'}(i\omega_n) \quad (11)$$

This accounts for the dressing of phonons by generic low-energy spin excitations; it is more general than the formation of magnon-polarons, since well-defined magnetic quasiparticles are not required. A full derivation and numerical estimates of $\eta_q^{\nu\nu'}$ from the ED bond correlations are presented in [70]. This calculation does not require broadening of the ED poles, allowing the absolute magnitude of κ_{xy} to be (roughly) estimated, as discussed below. The first term is proportional to a uniform magnetization, and represents the ‘‘Raman’’ couplings, which has negligible contribution in α -RuCl₃ due to the smallness of the \mathcal{L} interactions. The second term accounts for dissipationless scattering via \mathcal{A} (and \mathcal{G}) [47, 48], and has a more nuanced field-dependence. Together, they represent the total electronic Berry phase acquired under adiabatic atomic motion[67, 68, 70]. Skew-scattering of phonons[49, 50] corresponds to higher-order vertex corrections, and is not considered here.

To estimate the field-dependence of κ_{xy} , we numerically evaluated the phonon Berry curvature $\Omega_{q\nu}^{BC}$ resulting from the computed $\eta_q^{\nu\nu'}$. We find the Berry curvature of the acoustic phonons is proportional to $|q|$ for small momenta, and thus plot $\Omega_{q\nu}^{\theta} = \Omega_{q\nu}^{BC}/|q|$ in Fig. 3(a)-(c). Following[23, 48, 53, 86], at fixed temperature:

$$\kappa_{xy}^{ph} \propto - \sum_{\nu} \left(\frac{1}{c_{\nu}} \right)^3 \int_0^{2\pi} d\theta \Omega_{\nu}^{\theta} \quad (12)$$

where $c_{\nu} = \partial\omega_{q\nu}/\partial|q|$ is the speed of sound for each band, obtained from the *ab-initio* phonon calculations[70]. The qualitative evolution is depicted in Fig. 3(e) as $\kappa_{xy}^{ph}/|\kappa_{xy}^{\max}|$, i.e. normalized by the maximum value. For $B > B_c$, κ_{xy}^{ph} rapidly increases, reaches a maximum near 11 T, and then decays with increasing field. By varying the in-plane field direction, we also find that the sign structure of κ_{xy}^{ph} matches experimental observations, as detailed in [70].

There are several immediate observations. First, a magnetic field $B||a$ does induce a finite κ_{xy}^{ph} , revealing the *planar* phonon THE exists in α -RuCl₃. Second, while spin-phonon scattering is generally enhanced in the vicinity of B_c , the maximum in κ_{xy}^{ph} occurs in the asymptotically polarized phase (at 11 T). This can ultimately be traced to the nuances of the Hall viscosity and its relationship to the bond susceptibilities; the interband matrix elements $\eta_q^{\nu\nu'}$ change sign at B_c over much of the Brillouin zone, and only reach a maximum magnitude within the polarized phase[70]. In the off-shell approximation, $\kappa_{xy}^{ph} \propto \eta^3 \sim (\mathcal{A}/\Delta_s)^6$, where \mathcal{A} is the spin-phonon coupling, and Δ_s is the spin-gap. The phonon

Hall conductivity is therefore rapidly suppressed at high field due to the field-induced spin gap. Although ED likely overestimates the width of the peak in κ_{xy} , this finding is consistent with experiments, which report maxima in κ_{xy} in the range 8 - 12 T [2, 3, 7–10]. Lastly, we address the magnitude of $\kappa_{xy}^{\text{ph}}(T)$, which we estimate from the $T = 0$ ED bond correlations. In this approximation, $\kappa_{xy}^{\text{ph}}/T \propto T^3$. Per 2D layer, we obtain a peak value of $0.22 \kappa_{Q/2}$ for $T = 6$ K and $1.05 \kappa_{Q/2}$ for $T = 10$ K, where $\kappa_{Q/2} = \pi k_{\text{B}}^2/12\hbar$ is the half-quantum of thermal conductance. While a precise calculation should account for the temperature dependence of η_q , we find that the order of magnitude is compatible with experiments. On this basis, we conclude that phononic contributions likely represent a significant portion of the observed κ_{xy} in α -RuCl₃, and reproduce all essential experimental features.

In summary, taking careful account of the effects of microscopic spin-phonon couplings reveals that the phonon Hall effect is consistent with the low-temperature $\kappa_{xy}(B)$ in α -RuCl₃. The lack of contribution to κ_{xy} proportional to the magnetization is due to the smallness of the \mathcal{L} couplings. This holds for α -RuCl₃ because there are no low-lying electronic multiplets, but may not be true for other materials, such as $3d$ ferromagnets VI₃ [13] and FeCl₂ [14], where gaps between spin-orbit multiplets are significantly smaller. A full quantitative theory of phononic κ_{xy} capturing all intrinsic effects will require computing full q -, T -, and B -dependent spin correlations, retaining the ω -dependence of the self-energy, and including skew-scattering vertex corrections. While these elaborations are being pursued, the present results highlight a significant utility of first-principles spin-phonon coupling methods in elucidating the nature of the THE in specific materials.

The authors acknowledge discussions with M. Ye, L. Mangeolle, L. Savary, L. Balents, A. Nevidomskyy, S. Ren, D. Vanderbilt, L. Taillefer, and L. Chen. This research was funded by the Center for Functional Materials at WFU through a pilot grant, and Oak Ridge Associated Universities (ORAU) through the Ralph E. Powe Junior Faculty Enhancement Award to S.M.W. Part of the computations were performed using the Wake Forest University (WFU) High Performance Computing Facility [87], a centrally managed computational resource available to WFU researchers including faculty, staff, students, and collaborators. D.A.S.K. and R.V. gratefully acknowledge support by the Deutsche Forschungsgemeinschaft (DFG, German Research Foundation) for funding through TRR 288—422213477 (project A05).

* winters@wfu.edu

[1] Y. Kasahara, K. Sugii, T. Ohnishi, M. Shimozawa, M. Yamashita, N. Kurita, H. Tanaka, J. Nasu, Y. Mo-

- tome, T. Shibauchi, et al., Phys. Rev. Lett. **120**, 217205 (2018).
- [2] Y. Kasahara, T. Ohnishi, Y. Mizukami, O. Tanaka, S. Ma, K. Sugii, N. Kurita, H. Tanaka, J. Nasu, Y. Motome, et al., Nature **559**, 227 (2018).
- [3] T. Yokoi, S. Ma, Y. Kasahara, S. Kasahara, T. Shibauchi, N. Kurita, H. Tanaka, J. Nasu, Y. Motome, C. Hickey, et al., Science **373**, 568 (2021).
- [4] K. Imamura, S. Suetsugu, Y. Mizukami, Y. Yoshida, K. Hashimoto, K. Ohtsuka, Y. Kasahara, N. Kurita, H. Tanaka, P. Noh, et al., Sci. Adv. **10**, eadk3539 (2024).
- [5] R. Hentrich, M. Roslova, A. Isaeva, T. Doert, W. Brenig, B. Büchner, and C. Hess, Phys. Rev. B **99**, 085136 (2019).
- [6] É. Lefrançois, G. Grissonnanche, J. Baglo, P. Lampen-Kelley, J.-Q. Yan, C. Balz, D. Mandrus, S. Nagler, S. Kim, Y.-J. Kim, et al., Phys. Rev. X **12**, 021025 (2022).
- [7] J. Bruin, R. Claus, Y. Matsumoto, N. Kurita, H. Tanaka, and H. Takagi, Nat. Phys. **18**, 401 (2022).
- [8] Y. Kasahara, S. Suetsugu, T. Asaba, S. Kasahara, T. Shibauchi, N. Kurita, H. Tanaka, and Y. Matsuda, Phys. Rev. B **106**, L060410 (2022).
- [9] P. Czajka, T. Gao, M. Hirschberger, P. Lampen-Kelley, A. Banerjee, N. Quirk, D. G. Mandrus, S. E. Nagler, and N. P. Ong, Nat. Mater. **22**, 36 (2023).
- [10] H. Zhang, M. A. McGuire, A. F. May, H.-Y. Chao, Q. Zheng, M. Chi, B. C. Sales, D. G. Mandrus, S. E. Nagler, H. Miao, et al., Phys. Rev. Mater. **8**, 014402 (2024).
- [11] X.-T. Zhang, Y. H. Gao, and G. Chen, Phys. Rep. **1070**, 1 (2024).
- [12] T. Ideue, T. Kurumaji, S. Ishiwata, and Y. Tokura, Nat. Mater. **16**, 797 (2017).
- [13] H. Zhang, C. Xu, C. Carnahan, M. Sretenovic, N. Suri, D. Xiao, and X. Ke, Phys. Rev. Lett. **127**, 247202 (2021).
- [14] C. Xu, C. Carnahan, H. Zhang, M. Sretenovic, P. Zhang, D. Xiao, and X. Ke, Phys. Rev. B **107**, L060404 (2023).
- [15] C. Xu, H. Zhang, C. Carnahan, P. Zhang, D. Xiao, and X. Ke, Phys. Rev. B **109**, 094415 (2024).
- [16] M. Gillig, X. Hong, C. Wellm, V. Kataev, W. Yao, Y. Li, B. Büchner, and C. Hess, Phys. Rev. Research **5**, 043110 (2023).
- [17] N. Li, R. Neumann, S. Guang, Q. Huang, J. Liu, K. Xia, X. Yue, Y. Sun, Y. Wang, Q. Li, et al., Phys. Rev. B **108**, L140402 (2023).
- [18] L. Chen, É. Lefrançois, A. Vallipuram, Q. Barthélemy, A. Ataie, W. Yao, Y. Li, and L. Taillefer, arXiv preprint arXiv:2309.17231 (2023).
- [19] S. Guang, N. Li, R. L. Luo, Q. Huang, Y. Wang, X. Yue, K. Xia, Q. Li, X. Zhao, G. Chen, et al., Phys. Rev. B **107**, 184423 (2023).
- [20] X. Zhou, W. Wu, Y. Sui, Y.-f. Yang, and J. Luo, Adv. Funct. Mater. p. 2304921 (2024).
- [21] H.-L. Kim, T. Saito, H. Yang, H. Ishizuka, M. J. Coak, J. H. Lee, H. Sim, Y. S. Oh, N. Nagaosa, and J.-G. Park, Nat. Commun. **15**, 243 (2024).
- [22] A. Kitaev, Annals of Physics **321**, 2 (2006).
- [23] H. Katsura, N. Nagaosa, and P. A. Lee, Phys. Rev. Lett. **104**, 066403 (2010).
- [24] J. Nasu, J. Yoshitake, and Y. Motome, Phys. Rev. Lett.

- 119**, 127204 (2017).
- [25] P. McClarty, X.-Y. Dong, M. Gohlke, J. Rau, F. Pollmann, R. Moessner, and K. Penc, *Phys. Rev. B* **98**, 060404 (2018).
- [26] E. Z. Zhang, L. E. Chern, and Y. B. Kim, *Phys. Rev. B* **103**, 174402 (2021).
- [27] L. E. Chern, E. Z. Zhang, and Y. B. Kim, *Phys. Rev. Lett.* **126**, 147201 (2021).
- [28] S. Li and S. Okamoto, *Phys. Rev. B* **106**, 024413 (2022).
- [29] T. Saito, K. Misaki, H. Ishizuka, and N. Nagaosa, *Phys. Rev. Lett.* **123**, 255901 (2019).
- [30] B. Flebus and A. MacDonald, *Phys. Rev. B* **105**, L220301 (2022).
- [31] B. Flebus and A. MacDonald, *Phys. Rev. Lett.* **131**, 236301 (2023).
- [32] K. Sun, Z. Gao, and J.-S. Wang, *Phys. Rev. B* **103**, 214301 (2021).
- [33] M. Mori, A. Spencer-Smith, O. P. Sushkov, and S. Maekawa, *Phys. Rev. Lett.* **113**, 265901 (2014).
- [34] H. Guo and S. Sachdev, *Phys. Rev. B* **103**, 205115 (2021).
- [35] X.-Q. Sun, J.-Y. Chen, and S. A. Kivelson, *Phys. Rev. B* **106**, 144111 (2022).
- [36] H. Guo, D. G. Joshi, and S. Sachdev, *Proc. Natl. Acad. Sci. U.S.A.* **119**, e2215141119 (2022).
- [37] X. Zhang, Y. Zhang, S. Okamoto, and D. Xiao, *Phys. Rev. Lett.* **123**, 167202 (2019).
- [38] E. Thingstad, A. Kamra, A. Brataas, and A. Sudbø, *Phys. Rev. Lett.* **122**, 107201 (2019).
- [39] S. Park and B.-J. Yang, *Phys. Rev. B* **99**, 174435 (2019).
- [40] B. Sheikhi, M. Kargarian, and A. Langari, *Phys. Rev. B* **104**, 045139 (2021).
- [41] H. Huang and Z. Tian, *Phys. Rev. B* **104**, 064305 (2021).
- [42] S. Bao, Z.-L. Gu, Y. Shangguan, Z. Huang, J. Liao, X. Zhao, B. Zhang, Z.-Y. Dong, W. Wang, R. Kajimoto, et al., *Nat. Commun.* **14**, 6093 (2023).
- [43] D.-Q. To, C. Ameyaw, A. Suresh, S. Bhatt, M. Ku, M. Jungfleisch, J. Xiao, J. Zide, B. Nikolić, and M. Doty, *Phys. Rev. B* **108**, 085435 (2023).
- [44] L. Sheng, D. Sheng, and C. Ting, *Phys. Rev. Lett.* **96**, 155901 (2006).
- [45] J.-S. Wang and L. Zhang, *Phys. Rev. B* **80**, 012301 (2009).
- [46] L. Zhang, J. Ren, J.-S. Wang, and B. Li, *Phys. Rev. Lett.* **105**, 225901 (2010).
- [47] M. Ye, R. M. Fernandes, and N. B. Perkins, *Phys. Rev. Research* **2**, 033180 (2020).
- [48] M. Ye, L. Savary, and L. Balents, *arXiv preprint arXiv:2103.04223* (2021).
- [49] L. Mangeolle, L. Balents, and L. Savary, *Phys. Rev. X* **12**, 041031 (2022).
- [50] L. Mangeolle, L. Balents, and L. Savary, *Phys. Rev. B* **106**, 245139 (2022).
- [51] Y. Zhang, Y. Teng, R. Samajdar, S. Sachdev, and M. S. Scheurer, *Phys. Rev. B* **104**, 035103 (2021).
- [52] S. Singh, P. P. Stavropoulos, and N. B. Perkins, *arXiv preprint arXiv:2407.07990* (2024).
- [53] S. Li, H. Yan, and A. H. Nevidomskyy, *arXiv preprint arXiv:2301.07401* (2023).
- [54] R. Hentrich, A. U. Wolter, X. Zotos, W. Brenig, D. Nowak, A. Isaeva, T. Doert, A. Banerjee, P. Lampen-Kelley, D. G. Mandrus, et al., *Phys. Rev. Lett.* **120**, 117204 (2018).
- [55] S. Gass, P. M. Cónsoli, V. Kocsis, L. T. Corredor, P. Lampen-Kelley, D. G. Mandrus, S. E. Nagler, L. Janssen, M. Vojta, B. Büchner, et al., *Phys. Rev. B* **101**, 245158 (2020).
- [56] R. Schönemann, S. Imajo, F. Weickert, J. Yan, D. G. Mandrus, Y. Takano, E. L. Brosha, P. F. S. Rosa, S. E. Nagler, K. Kindo, et al., *Phys. Rev. B* **102**, 214432 (2020), ISSN 2469-9950, 2469-9969.
- [57] H. Li, T. Zhang, A. Said, G. Fabbris, D. G. Mazzone, J. Yan, D. Mandrus, G. B. Halász, S. Okamoto, S. Murakami, et al., *Nat. Commun.* **12**, 3513 (2021).
- [58] V. Kocsis, D. A. S. Kaib, K. Riedl, S. Gass, P. Lampen-Kelley, D. G. Mandrus, S. E. Nagler, N. Pérez, K. Nielsch, B. Büchner, et al., *Phys. Rev. B* **105**, 094410 (2022), ISSN 2469-9950, 2469-9969.
- [59] C. Kane and M. P. Fisher, *Phys. Rev. B* **55**, 15832 (1997).
- [60] N. Read and D. Green, *Phys. Rev. B* **61**, 10267 (2000).
- [61] M. Banerjee, M. Heiblum, V. Umansky, D. E. Feldman, Y. Oreg, and A. Stern, *Nature* **559**, 205 (2018).
- [62] J. Van Vleck, *Phys. Rev.* **57**, 426 (1940).
- [63] R. Orbach, *Proc. R. Soc. Lond. Ser. A-Contain. Pap. Math. Phys.* **264**, 458 (1961).
- [64] T. Ray and D. Ray, *Phys. Rev.* **164**, 420 (1967).
- [65] H. Capellmann and S. Lipinski, *Z. Phys. B: Condens. Matter* **83**, 199 (1991).
- [66] A. Iosevich and H. Capellmann, *Phys. Rev. B* **51**, 11446 (1995).
- [67] J. Bonini, S. Ren, D. Vanderbilt, M. Stengel, C. E. Dreyer, and S. Coh, *Phys. Rev. Lett.* **130**, 086701 (2023).
- [68] S. Ren, J. Bonini, M. Stengel, C. E. Dreyer, and D. Vanderbilt, *Phys. Rev. X* **14**, 011041 (2024).
- [69] R. Dhakal, S. Griffith, K. Choi, and S. M. Winter, *arXiv preprint arXiv:2407.00659* (2024).
- [70] See supplemental material, which contains references [88–114], for description of ab-initio methods, choice of phonon gauges, derivation of phonon thermal transport and Hall viscosity terms, further details of numerical evaluations of κ_{xx} and κ_{xy} , the field-angle dependence of κ_{xy} , and notes on low- q scaling of spin-phonon couplings, **G** and **L** couplings, and $q = 0$ optical phonon couplings.
- [71] J. G. Rau, E. K.-H. Lee, and H.-Y. Kee, *Phys. Rev. Lett.* **112**, 077204 (2014).
- [72] S. M. Winter, Y. Li, H. O. Jeschke, and R. Valentí, *Phys. Rev. B* **93**, 214431 (2016).
- [73] H.-S. Kim and H.-Y. Kee, *Phys. Rev. B* **93**, 155143 (2016).
- [74] R. Yadav, N. A. Bogdanov, V. M. Katukuri, S. Nishimoto, J. Van Den Brink, and L. Hozoi, *Sci. Rep.* **6**, 37925 (2016).
- [75] K. Ran, J. Wang, W. Wang, Z.-Y. Dong, X. Ren, S. Bao, S. Li, Z. Ma, Y. Gan, Y. Zhang, et al., *Phys. Rev. Lett.* **118**, 107203 (2017).
- [76] S. M. Winter, K. Riedl, P. A. Maksimov, A. L. Chernyshev, A. Honecker, and R. Valentí, *Nat. Commun.* **8**, 1152 (2017).
- [77] C. Eichstaedt, Y. Zhang, P. Laurell, S. Okamoto, A. G. Eguiluz, and T. Berlijn, *Phys. Rev. B* **100**, 075110 (2019).
- [78] P. Laurell and S. Okamoto, *npj Quantum Mater.* **5**, 2 (2020).
- [79] D. A. Kaib, K. Riedl, A. Razpopov, Y. Li, S. Backes,

- I. I. Mazin, and R. Valentí, npj Quantum Mater. **7**, 75 (2022).
- [80] P. Maksimov and A. Chernyshev, Phys. Rev. Research **2**, 033011 (2020).
- [81] S. Reschke, F. Mayr, Z. Wang, S.-H. Do, K.-Y. Choi, and A. Loidl, Phys. Rev. B **96**, 165120 (2017).
- [82] T. T. Mai, A. McCreary, P. Lampen-Kelley, N. Butch, J. R. Simpson, J.-Q. Yan, S. E. Nagler, D. Mandrus, A. H. Walker, and R. V. Aguilar, Phys. Rev. B **100**, 134419 (2019).
- [83] B. W. Lebert, S. Kim, D. A. Prishchenko, A. A. Tsirlin, A. H. Said, A. Alatas, and Y.-J. Kim, Phys. Rev. B **106**, L041102 (2022).
- [84] I. A. Leahy, C. A. Pocs, P. E. Siegfried, D. Graf, S.-H. Do, K.-Y. Choi, B. Normand, and M. Lee, Phys. Rev. Lett. **118**, 187203 (2017).
- [85] Y. Yu, Y. Xu, K. Ran, J. Ni, Y. Huang, J. Wang, J. Wen, and S. Li, Phys. Rev. Lett. **120**, 067202 (2018).
- [86] T. Qin, J. Zhou, and J. Shi, Phys. Rev. B **86**, 104305 (2012).
- [87] Information Systems and Wake Forest University, *WFU High Performance Computing Facility* (2021), URL <https://hpc.wfu.edu>.
- [88] G. Kresse and J. Furthmüller, Phys. Rev. B **54**, 11169 (1996).
- [89] G. Kresse and J. Furthmüller, Comput. Mater. Sci. **6**, 15 (1996).
- [90] G. Kresse and J. Hafner, Phys. Rev. B **47**, 558 (1993).
- [91] J. P. Perdew, K. Burke, and M. Ernzerhof, Phys. Rev. Lett. **77**, 3865 (1996).
- [92] G. Kresse and D. Joubert, Phys. Rev. B **59**, 1758 (1999).
- [93] P. E. Blöchl, Phys. Rev. B **50**, 17953 (1994).
- [94] S. Grimme, J. Antony, S. Ehrlich, and H. Krieg, J. Chem. Phys. **132** (2010).
- [95] D. Wood and A. Zunger, J. Phys. A Math. Gen. **18**, 1343 (1985).
- [96] P. Pulay, Chem. Phys. Lett. **73**, 393 (1980).
- [97] A. Liechtenstein, V. I. Anisimov, and J. Zaanen, Phys. Rev. B **52**, R5467 (1995).
- [98] G. Kresse, J. Furthmüller, and J. Hafner, Europhys. Lett. **32**, 729 (1995).
- [99] K. Parlinski, Z. Li, and Y. Kawazoe, Phys. Rev. Lett. **78**, 4063 (1997).
- [100] A. Togo, L. Chaput, T. Tadano, and I. Tanaka, J. Phys. Condens. Matter **35**, 353001 (2023).
- [101] A. Togo, J. Phys. Soc. Jpn. **92**, 012001 (2023).
- [102] I. Opahle, K. Koepernik, and H. Eschrig, Phys. Rev. B **60**, 14035 (1999).
- [103] K. Koepernik, O. Janson, Y. Sun, and J. Van Den Brink, Phys. Rev. B **107**, 235135 (2023).
- [104] S. Sugano, Y. Tanabe, and H. Kamimura, eds., *Multiplets of Transition-Metal Ions in Crystals*, vol. 33 of *Pure and Applied Physics* (Elsevier, 1970).
- [105] L. J. Sandilands, Y. Tian, A. A. Reijnders, H.-S. Kim, K. W. Plumb, Y.-J. Kim, H.-Y. Kee, and K. S. Burch, Phys. Rev. B **93**, 075144 (2016).
- [106] L. J. Sandilands, C. H. Sohn, H. J. Park, S. Y. Kim, K. W. Kim, J. A. Sears, Y.-J. Kim, and T. W. Noh, Phys. Rev. B **94**, 195156 (2016).
- [107] B. W. Lebert, S. Kim, B. H. Kim, S. H. Chun, D. Casa, J. Choi, S. Agrestini, K. Zhou, M. Garcia-Fernandez, and Y.-J. Kim, Phys. Rev. B **108**, 155122 (2023).
- [108] A. Togo, J. Phys. Soc. Jpn. **92**, 012001 (2023).
- [109] L. J. Sandilands, Y. Tian, K. W. Plumb, Y.-J. Kim, and K. S. Burch, Phys. Rev. Lett. **114**, 147201 (2015).
- [110] S. Chaudhary, D. M. Juraschek, M. Rodriguez-Vega, and G. A. Fiete, arXiv preprint arXiv:2306.11630 (2023).
- [111] R. Matsumoto, R. Shindou, and S. Murakami, Phys. Rev. B **89**, 054420 (2014).
- [112] H. Kondo, Y. Akagi, and H. Katsura, Progress of Theoretical and Experimental Physics **2020**, 12A104 (2020).
- [113] S. Toth and B. Lake, J. Phys. Condens. Matter **27**, 166002 (2015).
- [114] T. Kurumaji, Phys. Rev. Research **5**, 023138 (2023).

SUPPLEMENTAL MATERIAL

S1. Structure Relaxation and Phonons

In this section, we describe the computational details of structural relaxation and phonon calculations. For this purpose, the Vienna *Ab Initio* Simulation Package (VASP) [88–90] was used for the DFT calculations with PBE-GGA [91] exchange correlation functional. The Projector augmented wave (PAW) pseudopotential [92, 93] was implemented for the given elements as provided in VASP. To account the van der Waals interaction, we used the DFT-D3 method of Grimme with zero-damping function [94] and for the electronic minimization algorithm, we choose a mixture of the blocked-Davidson and RMM-DIIS algorithms [95, 96]. To approximately treat the strongly correlated *d*-electrons, we employed the rotationally invariant DFT+U of Liechtenstein *et al.* [97] with $U = 1.80$ eV and $J = 0.40$ eV on *d* orbitals of Ru atoms (method adapted from [83]).

We first relaxed an idealized structure of α -RuCl₃ with AA stacking in the space group $P\bar{3}1m$, starting from a similar out-of-plane layer-to-layer distance as observed in the reported $R\bar{3}$ structure. The relaxation was performed with an initial antiferromagnetic (Neél) spin configuration on the Ru sites. A k-mesh sampling of $8 \times 8 \times 8$ was chosen for the first Brillouin zone and the structural relaxation was performed until the forces were less than 0.005 eV/Å. The resulting structure is depicted in Fig. 4, and has a *c*-axis lattice constant of 5.7389 Å and in-plane lattice constant of 6.0577 Å.

To carry out the phonon calculations, we prepared a super-cell of $2 \times 2 \times 2$ and utilized the finite displacement method [98, 99] as implemented in Phonopy [100, 101]. Here, we chose a less dense k-mesh of $4 \times 4 \times 4$ due to the reduced Brillouin zone size of supercell.

S2. Details of Spin-Phonon Coupling Calculations

In order to estimate the spin-phonon couplings, we first start with an electronic Hamiltonian including linear electron-phonon coupling, which takes the form $\mathcal{H} = \mathcal{H}_{1p} + \mathcal{H}_{2p} + \mathcal{H}_{\text{el-ph}}$. We consider a basis of *d*-orbital Wannier functions on each Ru site. Formally, the one-particle Hamiltonian includes intersite hopping, intrasite crystal field, and spin-orbit coupling, $\mathcal{H}_{1p} = \mathcal{H}_{\text{hop}} + \mathcal{H}_{\text{CF}} + \mathcal{H}_{\text{SO}}$:

$$\mathcal{H}_{\text{hop}} = \sum_{ij\alpha\beta\sigma} t_{ij}^{\alpha\beta} c_{i,\alpha,\sigma}^\dagger c_{j,\beta,\sigma} \quad (13)$$

$$\mathcal{H}_{\text{CF}} = \sum_{i\alpha\beta\sigma} d_i^{\alpha\beta} c_{i,\alpha,\sigma}^\dagger c_{i,\beta,\sigma} \quad (14)$$

$$\mathcal{H}_{\text{SO}} = \sum_{i\alpha\beta\sigma\sigma'} \lambda_{\text{Ru}} \langle \phi_i^\alpha(\sigma) | \mathbf{L} \cdot \mathbf{S} | \phi_i^\beta(\sigma') \rangle c_{i,\alpha,\sigma}^\dagger c_{i,\beta,\sigma'} \quad (15)$$

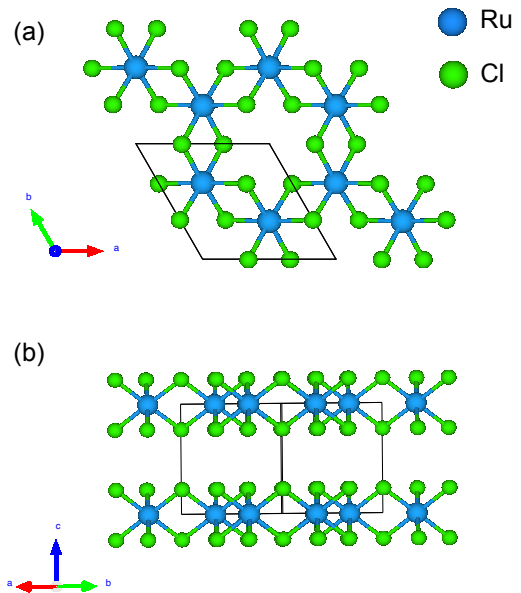


FIG. 4. Relaxed high-symmetry crystal structure of α -RuCl₃ with the $P\bar{3}1m$ symmetry (a) view along *c*-axis showing honeycomb planes. (b) side view showing AA stacking. Ru and Cl atoms are shown in blue and green colors respectively.

where $c_{i,\alpha,\sigma}^\dagger$ creates an electron at Ru site *i*, in *d*-orbital α , with spin σ . In order to estimate all of the one-particle terms, we perform fully relativistic density functional theory calculations on a $2 \times 2 \times 1$ supercell of the relaxed $P\bar{3}1m$ structure using FPLO [102], and project [103] the resulting Kohn-Sham bands onto Ru *d*-orbitals to obtain the electronic Hamiltonian in terms of Ru Wannier functions. For this purpose, we employ the PBE functional [91], and a $6 \times 6 \times 1$ *k*-point mesh. For the two-particle terms, we consider on-site interactions:

$$\mathcal{H}_{2p} = \sum_{i\alpha\beta\gamma\delta} \sum_{\sigma\sigma'} U_{\alpha\beta\gamma\delta} c_{i,\alpha,\sigma}^\dagger c_{i,\beta,\sigma'}^\dagger c_{i,\gamma,\sigma} c_{i,\delta,\sigma'} \quad (16)$$

where $U_{\alpha\beta\gamma\delta}$ are parameterized by the Slater parameters $F_0^{dd}, F_2^{dd}, F_4^{dd}$, following the spherically symmetric approximation [104]. In terms of these parameters, the Kanamori parameters for the t_{2g} orbitals satisfy:

$$U_{t_{2g}} = F_0^{dd} + \frac{4}{49}(F_2^{dd} + F_4^{dd}) \quad (17)$$

$$J_{t_{2g}} = \frac{3}{49}F_2^{dd} + \frac{20}{441}F_4^{dd} \quad (18)$$

We use $U_{t_{2g}} = 2.58$ eV, $J_{t_{2g}} = 0.29$ eV, and $F_4^{dd} = (5/8)F_2^{dd}$, which are taken from previous theoretical estimates from constrained RPA [77], and roughly compatible with estimates from optical studies [105–107].

The linear electron-phonon Hamiltonian is given by:

$$\mathcal{H}_{\text{el-ph}} = \sum_{\alpha\ell n} \mathcal{H}_{\Delta}^{\alpha\ell n} \hat{u}_{\alpha}(\ell n) \quad (19)$$

$$\mathcal{H}_{\Delta}^{\alpha\ell n} = \sum_{i\sigma j\sigma'} \Delta_{i\sigma j\sigma'}^{\mu\nu;\ell\alpha n} c_{i,\mu,\sigma}^{\dagger} c_{j,\nu,\sigma'} \quad (20)$$

The phonon operator $\hat{u}_{\alpha}(\ell n)$ refers to displacement of atom n , in the unit cell labelled ℓ , in the direction $\alpha \in \{x, y, z\}$. The elements $\Delta_{i\sigma j\sigma'}^{\mu\nu;\ell\alpha n}$ refer to changes in the single-particle matrix elements due to such a displacement. In order to estimate the latter (in real-space), we take a supercell approach similar to that described in Ref. 108. We construct a $2 \times 2 \times 1$ supercell, and compute the changes in the single-particle terms between sites in the full supercell induced by small displacements of each atom in the parent primitive cell. For this purpose, we displace each atom along the cartesian x, y, z directions by $\pm 0.02 \text{ \AA}$, and perform a DFT calculation on each geometry using FPLO and Wannier projection. The changes in the hoppings are then obtained by taking finite differences of the Hamiltonians in the Wannier basis. Finally, each orbital in the supercell is translated back to the parent cell to identify the corresponding $\Delta_{i\sigma j\sigma'}^{\mu\nu;\ell\alpha n}$ term with respect to the primitive cell. This provides an estimate of the electron-phonon coupling associated with any pair of orbitals, and an atomic displacement within a supercell distance of one of those orbitals. This coupling falls off rapidly with distance between the orbital site and the displaced atom, such that a $2 \times 2 \times 1$ supercell suffices to capture the relevant effects within the monolayer.

In order to estimate the spin-phonon couplings, we employ the des Cloizeaux effective Hamiltonian (dCEH) approach outlined in Ref. [69]. In the real-space formulation, for each site or bond, and each phonon flavor ($\alpha\ell n$), the electron/phonon Hamiltonian \mathcal{H} is exactly diagonalized, and the resulting low-energy states projected onto ideal $j_{1/2}$ states with variable number of phonon quanta. From this we obtain the real-space spin-phonon couplings $\mathbf{G}_i^{\alpha\ell n}$, $\mathbb{A}_i^{\alpha\ell n}$, and $\mathbf{L}_i^{\alpha\ell n;\beta\ell m}$:

$$\begin{aligned} \mathcal{H}_{\text{sp}} = & \sum_{ij,\alpha\ell n} (\mathbf{S}_i \cdot \mathbb{A}_{ij}^{\alpha\ell n} \cdot \mathbf{S}_j) \hat{u}_{\alpha}(\ell n) \\ & + \sum_{i,\alpha\ell n} (\mathbf{G}_i^{\alpha\ell n} \cdot \mathbf{S}_i) \hat{p}_{\alpha}(\ell n) \\ & + \sum_{\substack{i \\ \alpha\ell n, \beta\ell m}} (\mathbf{L}_i^{\alpha\ell n;\beta\ell m} \cdot \mathbf{S}_i) \hat{u}_{\alpha}(\ell n) \hat{p}_{\beta}(\ell m) \quad (21) \end{aligned}$$

where $\hat{u}_{\alpha}(\ell n)$ refers to the displacement from equilibrium of the atom in unit cell ℓ with index n , in the $\alpha \in \{x, y, z\}$ direction; $\hat{p}_{\alpha}(\ell n)$ gives the corresponding atomic momentum.

In terms of q -space operators, the real-space atomic

displacement and momentum operators may be written:

$$\hat{u}_{\alpha}(\ell n) = \sqrt{\frac{\hbar}{2Nm_n}} \sum_{q\nu} \frac{e^{iq \cdot r_{\ell n}}}{\sqrt{\omega_{q\nu}}} u_{q\nu} e_{\alpha n}^{q\nu} \quad (22)$$

$$\hat{p}_{\alpha}(\ell n) = \sqrt{\frac{\hbar m_n}{2N}} \sum_{q\nu} \sqrt{\omega_{q\nu}} e^{iq \cdot r_{\ell n}} p_{q\nu} e_{\alpha n}^{q\nu} \quad (23)$$

where $\hat{u}_{\alpha}(\ell n)$ refers to the displacement of the n th atom in the ℓ th unit cell, in the $\alpha \in \{x, y, z\}$ direction. $r_{\ell n}$ is the position of such atom, m_n is its mass, and $e_{\alpha n}^{q\nu} = (e_{\alpha n}^{-q\nu})^*$ are the phonon eigenvectors associated with momentum q and band index ν . The latter are obtained from the ab-initio phonon calculations described above. The q -space couplings are then given by:

$$\mathbf{G}_{(i)}^{q\nu} = \sum_{\alpha\ell n} \sqrt{\frac{\hbar\omega_{q\nu}m_n}{2}} e_{\alpha n}^{q\nu} \mathbf{G}_i^{\alpha\ell n} e^{iq \cdot r_{\ell n}} \quad (24)$$

$$\mathbb{A}_{(ij)}^{q\nu} = \sum_{\alpha\ell n} \sqrt{\frac{\hbar}{2m_n\omega_{q\nu}}} e_{\alpha n}^{q\nu} \mathbb{A}_{ij}^{\alpha\ell n} e^{iq \cdot r_{\ell n}} \quad (25)$$

$$\begin{aligned} \mathbf{L}_{(i)}^{q\nu;-q\nu'} = & \frac{\hbar}{2} \sum_{\substack{\alpha\ell n \\ \beta\ell m}} \sqrt{\frac{m_n\omega_{q\nu'}}{m_n\omega_{q\nu}}} \left(e_{\alpha n}^{q\nu} e_{\beta m}^{-q\nu'} \cdot \right. \\ & \left. \mathbf{L}_i^{\alpha\ell n;\beta\ell m} e^{iq \cdot (r_{\ell n} - r_{\ell m})} \right) \quad (26) \end{aligned}$$

for N unit cells and phonon frequency $\omega_{q\nu}$. In order to estimate the full q - and band-dependence of the $\mathbb{A}_{(ij)}^{q\nu}$ couplings, we followed this approach using two-site clusters of Ru sites and including displacements of atoms within 4.0 \AA for the crystal field electron-phonon coupling, and 4.64 \AA of the bond center for the hopping electron-phonon terms. To mitigate spurious effects associated with the finite distance cutoff, we subtract from each electron-phonon coupling (separately for each direction α) the average value of $\Delta_{i\sigma j\sigma'}^{\mu\nu;\ell\alpha n}$ over the atoms included within the cutoff. This ensures that any uniform translation of all atoms under consideration corresponds to no modification of the Hamiltonian. The electron-phonon couplings fall off rapidly with distance, so this truncation does not introduce significant errors.

In order to estimate the \mathbf{G} and \mathbf{L} couplings, we employed a different approach explicitly in q -space. The advantage of this approach is that it mitigates errors accumulated over the summation of the real space spin-phonon couplings in the Fourier transform. Instead, the electron-phonon coupling is Fourier transformed to q -space, and the electron-phonon Hamiltonian is diagonalized for each momentum instead. In this case, the electron-phonon Hamiltonian can be written:

$$\mathcal{H}_{\text{el-ph}} = \sum_{q\nu} \mathcal{H}_{\Delta}^{q\nu} u_{q\nu} = \mathcal{H}_{\Delta}^{q\nu} a_{q\nu} + \mathcal{H}_{\Delta}^{-q\nu} a_{q\nu}^{\dagger} \quad (27)$$

$$\mathcal{H}_{\Delta}^{q\nu} = \sum_{\alpha\ell n} \sqrt{\frac{\hbar}{2Nm_n}} \frac{e^{iq \cdot r_{\ell n}}}{\sqrt{\omega_{q\nu}}} e_{\alpha n}^{q\nu} \mathcal{H}_{\Delta}^{\alpha\ell n} \quad (28)$$

where $\mathcal{H}_\Delta^{-q\nu} = (\mathcal{H}_\Delta^{q\nu})^\dagger$. The lowest order contribution to the \mathbf{G} coupling can then be obtained by diagonalizing a one-site cluster for each Ru site in the unit cell, with a Hamiltonian given in block form by:

$$\mathcal{H}_i = \left(\begin{array}{c|c} \mathcal{H}_{1p} + \mathcal{H}_{2p} & \mathcal{H}_\Delta^{q\nu} e^{-iq \cdot r_i} \\ \hline \mathcal{H}_\Delta^{-q\nu} e^{iq \cdot r_i} & \mathcal{H}_{1p} + \mathcal{H}_{2p} + \hbar\omega_{q\nu} \end{array} \right) \quad (29)$$

The low-energy effective Hamiltonian derived from the dCEH approach is then given by:

$$\mathcal{H}_{\text{low}} = \mathcal{H}_0 + \mathcal{H}_1 a_{q\nu}^\dagger a_{q\nu} + \mathcal{H}_+ a_{q\nu}^\dagger + \mathcal{H}_- a_{q\nu} \quad (30)$$

and the q -space operator is simply:

$$\mathcal{H}_G = i \sum_{q\nu, i} (a_{-q\nu}^\dagger - a_{q\nu}) \mathcal{G}_{(i)}^{q\nu} \quad (31)$$

$$\mathcal{G}_{(i)}^{q\nu} = i \mathcal{H}_- \quad (32)$$

This calculation is repeated for each q , ν , and site i of interest. Computing the lowest order contribution to the \mathbf{L} couplings instead requires two calculations for each band and momentum. The associated Hamiltonian can be expanded as:

$$\mathcal{H}_L = i \sum_{q\nu\nu'} (a_{-q\nu}^\dagger + a_{q\nu}) (a_{q\nu'}^\dagger - a_{-q\nu'}) \mathcal{L}_{(i)}^{q\nu; -q\nu'} \quad (33)$$

Due to the mixed $-q$ and q operators, we perform two separate diagonalizations of the electronic Hamiltonian.

In the first calculation, we diagonalize:

$$\mathcal{H}_i = \left(\begin{array}{c|c|c|c} \mathcal{H}_{1p} + \mathcal{H}_{2p} & \mathcal{H}_\Delta^{q\nu} e^{-iq \cdot r_i} & \mathcal{H}_\Delta^{q\nu'} e^{-iq \cdot r_i} & 0 \\ \hline \mathcal{H}_\Delta^{-q\nu} e^{iq \cdot r_i} & \mathcal{H}_{1p} + \mathcal{H}_{2p} + \hbar\omega_{q\nu} & 0 & \mathcal{H}_\Delta^{q\nu'} e^{-iq \cdot r_i} \\ \hline \mathcal{H}_\Delta^{-q\nu'} e^{iq \cdot r_i} & 0 & \mathcal{H}_{1p} + \mathcal{H}_{2p} + \hbar\omega_{q\nu'} & \mathcal{H}_\Delta^{q\nu} e^{-iq \cdot r_i} \\ \hline 0 & \mathcal{H}_\Delta^{-q\nu'} e^{iq \cdot r_i} & \mathcal{H}_\Delta^{-q\nu} e^{iq \cdot r_i} & \mathcal{H}_{1p} + \mathcal{H}_{2p} + \hbar(\omega_{q\nu} + \omega_{q\nu'}) \end{array} \right) \quad (34)$$

for which the low-energy Hamiltonian corresponds to:

$$\begin{aligned} \mathcal{H}_{\text{low}}^a = & \mathcal{H}_0^a + \mathcal{H}_1^{a\nu} a_{q\nu}^\dagger a_{q\nu} + \mathcal{H}_+^{a\nu} a_{q\nu}^\dagger + \mathcal{H}_-^{a\nu} a_{q\nu} + \mathcal{H}_1^{a\nu'} a_{q\nu'}^\dagger a_{q\nu'} + \mathcal{H}_+^{a\nu'} a_{q\nu'}^\dagger + \mathcal{H}_-^{a\nu'} a_{q\nu'} \\ & + \mathcal{H}_{++}^{a\nu\nu'} a_{q\nu}^\dagger a_{q\nu'}^\dagger + \mathcal{H}_{-+}^{a\nu\nu'} a_{q\nu}^\dagger a_{q\nu'}^\dagger + \mathcal{H}_{+-}^{a\nu\nu'} a_{q\nu}^\dagger a_{q\nu'} + \mathcal{H}_{--}^{a\nu\nu'} a_{q\nu} a_{q\nu'} + \mathcal{O}(a^3) \end{aligned} \quad (35)$$

In the second calculation, we diagonalize:

$$\mathcal{H}_i = \left(\begin{array}{c|c|c|c} \mathcal{H}_{1p} + \mathcal{H}_{2p} & \mathcal{H}_\Delta^{q\nu} e^{-iq \cdot r_i} & \mathcal{H}_\Delta^{-q\nu'} e^{iq \cdot r_i} & 0 \\ \hline \mathcal{H}_\Delta^{-q\nu} e^{iq \cdot r_i} & \mathcal{H}_{1p} + \mathcal{H}_{2p} + \hbar\omega_{q\nu} & 0 & \mathcal{H}_\Delta^{-q\nu'} e^{iq \cdot r_i} \\ \hline \mathcal{H}_\Delta^{q\nu'} e^{-iq \cdot r_i} & 0 & \mathcal{H}_{1p} + \mathcal{H}_{2p} + \hbar\omega_{q\nu'} & \mathcal{H}_\Delta^{q\nu} e^{-iq \cdot r_i} \\ \hline 0 & \mathcal{H}_\Delta^{q\nu'} e^{-iq \cdot r_i} & \mathcal{H}_\Delta^{-q\nu} e^{iq \cdot r_i} & \mathcal{H}_{1p} + \mathcal{H}_{2p} + \hbar(\omega_{q\nu} + \omega_{q\nu'}) \end{array} \right) \quad (36)$$

for which the low-energy Hamiltonian corresponds to:

$$\begin{aligned} \mathcal{H}_{\text{low}}^b = & \mathcal{H}_0^b + \mathcal{H}_1^{b\nu} a_{q\nu}^\dagger a_{q\nu} + \mathcal{H}_+^{b\nu} a_{q\nu}^\dagger + \mathcal{H}_-^{b\nu} a_{q\nu} + \mathcal{H}_1^{b\nu'} a_{-q\nu'}^\dagger a_{-q\nu'} + \mathcal{H}_+^{b\nu'} a_{-q\nu'}^\dagger + \mathcal{H}_-^{b\nu'} a_{-q\nu'} \\ & + \mathcal{H}_{++}^{b\nu\nu'} a_{q\nu}^\dagger a_{-q\nu'}^\dagger + \mathcal{H}_{-+}^{b\nu\nu'} a_{q\nu}^\dagger a_{-q\nu'}^\dagger + \mathcal{H}_{+-}^{b\nu\nu'} a_{q\nu}^\dagger a_{-q\nu'} + \mathcal{H}_{--}^{b\nu\nu'} a_{q\nu} a_{-q\nu'} + \mathcal{O}(a^3) \end{aligned} \quad (37)$$

Then, by inspection,

$$\mathcal{L}_{(i)}^{q\nu; -q\nu'} = \frac{1}{2i} \left(\mathcal{H}_{-+}^{a\nu\nu'} - \mathcal{H}_{--}^{b\nu\nu'} \right) \quad (38)$$

These calculations are repeated for each q -point and pair of phonon bands. To extract the low momentum dependence of each coupling, we perform the calculations for different values of $|q| < 0.1$ reciprocal lattice units, and fit the computed couplings to the expected scaling form.

S3. Note on Phonon Gauges

In this section, we discuss the choice of gauge for the phonon eigenvectors of the acoustic modes. As depicted in Fig. 5, it is not possible for both the real and imaginary parts of the phonon eigenvectors to be continuous at both $q = 0$ and finite q . In the conventional gauge choice, employed in most *ab-initio* phonon codes, $\text{Im}[e_{\alpha n}^{q\nu}]$ vanishes in the limit $q \rightarrow 0$. In this case, it is necessary for the eigenvectors of the TA and LA modes to have branch

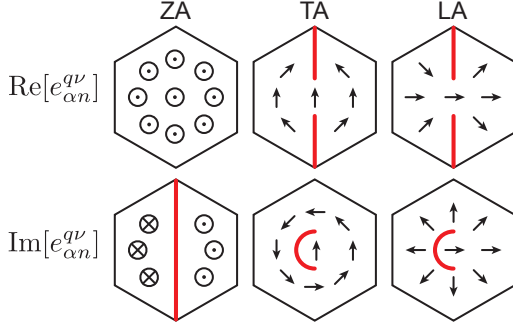


FIG. 5. Evolution of the real and imaginary parts of the phonon eigenvectors $e_{\alpha n}^{q\nu}$ for ZA, TA, and LA modes in the chosen gauge. Arrows indicate the dominant direction of atomic displacement corresponding to eigenvectors at different q -points in the Brillouin zone. Transforming the ZA eigenvectors to be purely real and the TA and LA eigenvectors to be purely imaginary in the limit $q \rightarrow 0$ ensures smooth spin-phonon couplings in the same limit.

cuts at finite q within the 2D Brillouin zone, leading to corresponding branch cuts in the spin-phonon couplings. For these modes, it is more convenient to make a gauge transformation that makes the eigenvectors continuous at all finite q . In general, the spin-phonon Hamiltonian is invariant under gauge transformations of the form:

$$a_{q\nu} e_{\alpha n}^{q\nu} \rightarrow a_{q\nu} e_{\alpha n}^{q\nu} e^{-i\phi_{q\nu}} \quad (39)$$

$$\mathcal{G}_{(i)}^{q\nu} \rightarrow \mathcal{G}_{(i)}^{q\nu} e^{i\phi_{q\nu}} \quad (40)$$

$$\mathcal{A}_{(ij)}^{q\nu} \rightarrow \mathcal{A}_{(ij)}^{q\nu} e^{i\phi_{q\nu}} \quad (41)$$

$$\mathcal{L}_{(i)}^{q\nu; q'\nu'} \rightarrow \mathcal{L}_{(i)}^{q\nu; q'\nu'} e^{i(\phi_{q\nu} + \phi_{q'\nu'})} \quad (42)$$

provided $\phi_{q\nu} = -\phi_{-q\nu}$. The eigenvectors of the TA and LA modes can be made continuous everywhere in the 2D Brillouin zone except exactly at $q = 0$ via a transformation that makes $e_{\alpha n}^{q\nu}$ primarily imaginary, such that $\lim_{q \rightarrow 0} \text{Re}[e_{\alpha n}^{q\nu}] = 0$. With this choice, the LA and TA modes at finite q become even under inversion (which takes $q \rightarrow -q$), while the ZA modes remain odd.

S4. Note on Low- q Scaling of Acoustic Mode Couplings

In this section, we discuss the low momentum scaling of the spin-phonon couplings. As noted in the previous section, the phonon eigenvectors satisfy $e_{\alpha n}^{q\nu} = (e_{\alpha n}^{-q\nu})^*$. For small q , we may expand the coefficients as:

$$e_{\alpha n}^{q\nu} e^{i\mathbf{q} \cdot \mathbf{r}_{\alpha n}} = a_{\alpha n}^{q\nu} + i\vec{b}_{\alpha n}^{q\nu} \cdot \vec{q} + \mathcal{O}(q^2) \quad (43)$$

$$a_{\alpha n}^{q\nu} = \text{Re}[a_{\alpha n}^{\nu}] + i \text{Im}[a_{\alpha n}^{\nu}] \text{sgn}(q) \quad (44)$$

$$\vec{b}_{\alpha n}^{q\nu} = \text{Re}[\vec{b}_{\alpha n}^{\nu}] + i \text{Im}[\vec{b}_{\alpha n}^{\nu}] \text{sgn}(q) \quad (45)$$

The gauge choice described in the previous section corresponds to choosing $a_{\alpha n}^{\nu}$ and $i\vec{b}_{\alpha n}^{q\nu}$ to be completely real

for the ZA modes and completely imaginary for the TA and LA modes. In the limit $q \rightarrow 0$, the couplings for the acoustic modes must vanish, since this corresponds to a uniform translation of the lattice. As a consequence,

$$\sum_{\alpha n} \sqrt{m_n} a_{\alpha n}^{q\nu} \mathbf{G}_i^{\alpha n} = 0 \quad (46)$$

$$\sum_{\alpha n} \frac{1}{\sqrt{m_n}} a_{\alpha n}^{q\nu} \mathbb{A}_{ij}^{\alpha n} = 0 \quad (47)$$

and separately:

$$\sum_{\alpha n} \frac{1}{\sqrt{m_n}} a_{\alpha n}^{q\nu} \mathbf{L}_i^{\alpha n; \beta k m} = 0 \quad (48)$$

$$\sum_{\beta k m} \sqrt{m_m} a_{\beta m}^{q\nu} \mathbf{L}_i^{\alpha n; \beta k m} = 0 \quad (49)$$

As a consequence, the acoustic phonon couplings scale with a factor of q for every phonon eigenvector appearing in their expression, in addition to any factors of ω_q . This leads to the scaling of the couplings:

$$\mathbb{A} \propto \frac{1}{\sqrt{\omega_q}} q \propto q^{1/2} \quad (50)$$

$$\mathbf{L} \propto q^2 \quad (51)$$

$$\mathbf{G} \propto \sqrt{\omega_q} q \propto q^{3/2} \quad (52)$$

Here, we have assumed that $\omega_q \propto q$. This is satisfied for all acoustic modes at sufficiently small $|q|$. We have verified that this scaling is satisfied in our numerical results.

S5. Note on Acoustic Phonon L- and G-Couplings

Here, we discuss the q -dependence of the \mathbf{L} and \mathbf{G} couplings for the acoustic modes. These couplings are sufficiently small in α -RuCl₃ as to have negligible consequence on the thermal transport. However, it is instructive to consider them in the context of other honeycomb materials.

At lowest order, the \mathbf{L} terms contribute to phonon chirality through a coupling to a uniform ($q = 0$) spin order parameter, which corresponds to $q' = -q$ in equation (3) of the main text. This represents the electronic contribution to the “two-phonon Raman” process discussed in [44–46]. Fig. 6(a-c) shows the computed momentum-dependence of $\mathbf{L}_{(i)}^{\theta\nu; \nu'}$. In the limit of small q , for the chosen gauge, the coupling is equal at both Ru sites in the unit cell. For $\nu = \nu'$, the coupling vanishes. Otherwise, the symmetry of \mathbf{L} is determined by the product of the coupled phonons. $\mathbf{L}_{ZA;TA}^{\theta}$ is even with respect to C_2 and odd with respect to m . $\mathbf{L}_{ZA;LA}^{\theta}$ is odd with respect to C_2 and even with respect to m . $\mathbf{L}_{TA;LA}^{\theta}$ is odd with respect to both C_2 and m . Within the chosen gauge, the leading contributions to $\mathbf{L}_{ZA;TA}^{\theta}$ and $\mathbf{L}_{ZA;LA}^{\theta}$ are imaginary, while $\mathbf{L}_{TA;LA}^{\theta}$ is real.

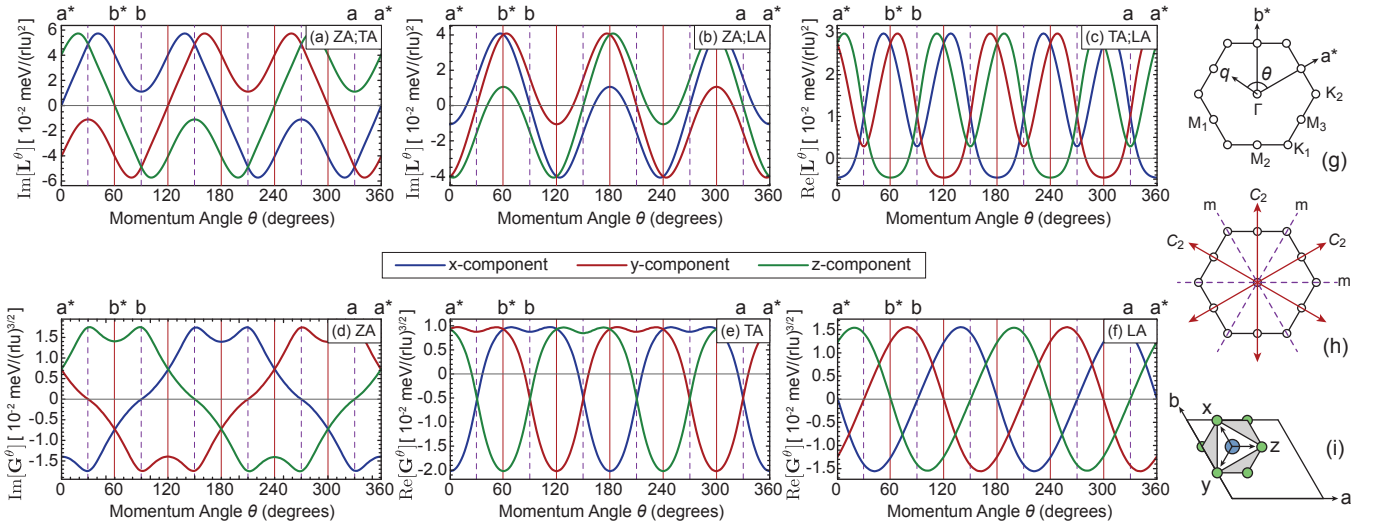


FIG. 6. Momentum angle dependence of the computed $\mathbf{L}_{(i)}^{\theta\nu;\nu'}$ and $\mathbf{G}_{(i)}^{\theta\nu}$ spin-phonon couplings. (a)-(c): (x, y, z) components of $\mathbf{L}_{(i)}^{\theta\nu;\nu'}$. The pairs of acoustic modes $\nu; \nu' = \text{ZA, TA, and LA}$ are labelled in the upper right of each panel. (d)-(e): (x, y, z) components of $\mathbf{G}_{(i)}^{\theta\nu}$. (g) first Brillouin zone showing the definition of a^* and b^* axes and θ (measured from the a^* axis). (h) orientation, in q -space, of the relevant symmetry operations for the single-site couplings. (i) Single Ru site showing definition of cubic axes.

The combinations of the symmetries and gauge choice ensure that the \mathbf{L} vectors wind around $q = 0$. For each combination of bands, there is a component of \mathbf{L} in the direction $\mathbf{u}_{q\nu} \times \mathbf{p}_{q\nu'}$. For example, the primary atomic motion for the LA mode is in-plane, parallel to q . The primary motion for the TA mode is in-plane, perpendicular to q . This leads to a component of $\mathbf{L}_{\text{TA;LA}}^\theta$ that points out of plane, corresponding to a spin-phonon coupling like $\mathbf{S} \cdot (\mathbf{u} \times \mathbf{p})$, which has been previously anticipated on phenomenological grounds[44]. However, we also find significant contributions to the θ -dependence of \mathbf{L} that depart from this form, which highlight the subtleties of spin-phonon coupling of spin-orbital moments.

It is insightful to consider the microscopic origin of the \mathbf{L} couplings. By performing calculations employing model electron-phonon couplings and idealized crystal fields, we find that the largest contribution to \mathbf{L} scales like $(\mathcal{H}_{\text{el-ph}})^2 / \lambda_{\text{Ru}}^2$. As detailed in section S9 below, the \mathbf{L} couplings represent the geometric phase the electronic wavefunction acquires under adiabatic motion of the nuclei. This occurs because the specific spin-orbital composition of the ground-state doublet at each site depends on the local crystal environment. The primary mechanism for this is mixing of the $j_{1/2}$ states with $j_{3/2}$ states. The relatively large value of the SOC constant λ_{Ru} reduces this effect in $\alpha\text{-RuCl}_3$. Thus, one can expect \mathbf{L} to be suppressed in materials with strong SOC or otherwise energetically separated single-ion states.

The momentum-dependence of the $\mathbf{G}_{(i)}^{\theta\nu}$ couplings are shown in Fig. 6(d-f). $\mathbf{G}_{\text{ZA}}^\theta$ is even with respect to m and odd with respect to C_2 . $\mathbf{G}_{\text{TA}}^\theta$ is odd with respect

to both symmetries. $\mathbf{G}_{\text{LA}}^\theta$ is even with respect to both symmetries. A smooth gauge requires $\lim_{q \rightarrow 0} \mathbf{G}_{\text{ZA}}$ to be completely imaginary, while $\lim_{q \rightarrow 0} \mathbf{G}_{\text{TA}}$ and \mathbf{G}_{LA} are completely real. As a consequence of these symmetries, the \mathbf{G} -vectors thus wind differently around the origin; \mathbf{G}_{ZA} winds once, while \mathbf{G}_{TA} and \mathbf{G}_{LA} wind twice in the opposite direction. The winding of \mathbf{G} is a generic feature of spin-phonon couplings, and is not unique to $\alpha\text{-RuCl}_3$.

As with the \mathbf{L} couplings, it is instructive to consider why the \mathbf{G} couplings are orders of magnitude smaller than the \mathbf{A} couplings. By performing calculations employing model electron-phonon couplings and idealized crystal fields, we find that the largest contribution to \mathbf{G} scales like $\mathcal{H}_{\text{el-ph}} J_H / \Delta_{t_2g-e_g}^2$. Here, $\Delta_{t_2g-e_g}$ is the splitting of the t_{2g} and e_g orbitals, and $J_H \propto F_2, F_4$ is the strength of Hund's coupling at the Ru site. The origin of this contribution can be seen as follows. Although the nominal electronic configuration of the $J_{\text{eff}} = 1/2$ single-ion ground state places four electrons in the $j_{3/2}$ single-particle spin-orbitals, and one electron in the $j_{1/2}$ orbital, the influence of the Coulomb interactions induces weight in configurations with finite occupancy of the e_g orbitals. This is true because of finite values of Coulomb integrals such as $U_{z^2,xy,yz,xz} = \langle d_{z^2} d_{xy} | e^2 / r_{12} | d_{yz} d_{xz} \rangle$ in the full spherically symmetric Coulomb tensor. Thus, the Coulomb interactions do not conserve separately the number electrons in the e_g and t_{2g} orbitals. Any phonon that modulates the mixing of t_{2g} and e_g orbitals can induce transitions between $m_J = +1/2$ and $m_J = -1/2$ states through the Coulomb-driven mixing of the t_{2g} and e_g configurations. However, because such effects in-

volve very small contributions to the ground-state moments (and mixing with excited electronic states of much higher energy), the modulation of the ground-state moment composition by the lattice motion is small.

S6. Note on Γ -point Symmetries and Optical Phonon Couplings

For a single layer of RuCl₃, there are in total 24 phonon bands. At $q = 0$, these decompose into $A_{2u} \oplus E_u$ for the acoustic modes and $2A_{1g} \oplus 2A_{2g} \oplus 4E_g \oplus A_{1u} \oplus 2A_{2u} \oplus 3E_u$ for the optical modes. All spin-phonon couplings must vanish for the acoustic bands at $q = 0$, but this is not the case for the optical bands. It is therefore instructive to consider which spin operators may couple to each mode.

For the \mathbb{A} couplings, the general forms for the $q = 0$ interaction matrices for the nearest-neighbor Z-bond are:

$$A_{1g}, E_g^a : \quad \mathbb{A}_{q=0}^Z = \begin{pmatrix} A & C & D \\ C & A & D \\ D & D & B \end{pmatrix} \quad (53)$$

$$A_{2g}, E_g^b : \quad \mathbb{A}_{q=0}^Z = \begin{pmatrix} A & 0 & B \\ 0 & -A & -B \\ B & -B & 0 \end{pmatrix} \quad (54)$$

$$A_{1u}, E_u^a : \quad \mathbb{A}_{q=0}^Z = \begin{pmatrix} 0 & 0 & A \\ 0 & 0 & A \\ -A & -A & 0 \end{pmatrix} \quad (55)$$

$$A_{2u}, E_u^b : \quad \mathbb{A}_{q=0}^Z = \begin{pmatrix} 0 & A & B \\ -A & 0 & -B \\ -B & B & 0 \end{pmatrix} \quad (56)$$

For the E_g modes, it is possible to take a linear combination of eigenvectors so that one of the modes has a coupling like A_{1g} , and the other A_{2g} for the Z-bond. Similarly, the basis for E_u modes can be constructed so that one couples via a matrix like A_{1u} and the other like A_{2u} . One can see that SOC significantly enriches the spin-phonon coupling. In the absence of SOC, all couplings must take the Heisenberg $J\mathbf{S}_i \cdot \mathbf{S}_j$ form, including the spin-phonon couplings, which represent $\partial J / \partial u$. As a consequence, $\mathbb{A}_{xy} = \mathbb{A}_{xz} = \mathbb{A}_{yz} = 0$, and $\mathbb{A}_{xx} = \mathbb{A}_{yy} = \mathbb{A}_{zz}$. With these restrictions, only the coupling to the A_{1g} and one of the E_g modes would be permitted by symmetry. In table I, we summarize the computed phonon energies and \mathbb{A} couplings for the $q = 0$ phonons. These couplings reveal two features. First, all \mathbb{A} matrices are strongly anisotropic, and vary widely between the different phonon modes. This is not surprising considering the spin-orbital moments in α -RuCl₃, and multiple exchange pathways. Different lattice displacements modulate different intersite hoppings, which affect different couplings. Second, we find that the spin-phonon couplings are relatively large, on the scale of several meV, which is essentially the scale of the bare magnetic couplings themselves. This suggests a significant possibility

TABLE I. Computed \mathbb{A} couplings for the nearest-neighbor Z-bonds for the optical $q = 0$ modes. The parameters A-D refer to equations (53) - (56). For the E modes, we have chosen a linear combination so that one mode has a coupling of the A_1 form and the other has the A_2 form.

Label	Energy (meV)		Components of $\mathbb{A}_{q=0,\nu}$ (meV)			
	Comp.	Exp.	A	B	C	D
E_g^{1a}	13.5	14.6[82]	-0.329	-2.238	-0.263	1.174
E_g^{1b}			0.149	-0.714		
A_{2u}^1	15.2	15.2[81]	0.524	1.276		
A_{2u}^2	15.8		0.349	-0.788		
E_g^{2a}	19.2	20.5[82]	0.298	-3.259	0.759	-0.179
E_g^{2b}			1.28	0.434		
E_u^{1a}	20.3	21.2[81]	0.265	-1.516		
E_u^{1b}			-0.179			
A_{1g}^1	23.7	27.5[82]	-0.202	-1.403	-0.56	-1.028
E_g^{3a}	28.5	33.6[82]	2.044	2.856	-1.615	-0.078
E_g^{3b}			-0.824	0.13		
E_u^{2a}	31.6		0.341	-0.362		
E_u^{2b}			0.003			
A_{2g}^2	33.0		0.082	-0.359		
E_g^{4a}	33.6	36.8[82]	-0.179	-0.497	-0.775	-0.043
E_g^{4b}			1.727	-0.103		
A_{2u}^2	33.6		0.594	0.832		
A_{1u}^1	36.8		0.104			
E_u^{3a}	37.4	~ 38 [81]	0.066	-1.174		
E_u^{3b}			0.077			
A_{1g}^2	37.6	37.5[82]	-0.843	1.896	1.009	0.071

for hybridizing the phonons and magnetic excitations, provided they overlap in energy. On the basis of previous Raman scattering studies[109], the lowest energy optical modes do overlap with a magnetic continuum, which extends up to $\sim 20 - 25$ meV. As a consequence of the spin-phonon coupling, we would expect the optical phonons to acquire a temperature-dependent self-energy contribution:

$$\Pi_{q,\nu}(i\nu_n) = - \int_0^\beta d\tau e^{i\nu_n\tau} \langle \mathcal{A}_{q\nu}(\tau) \mathcal{A}_{-q\nu}(0) \rangle \quad (57)$$

This would be expected to lead to both shifting and broadening of the phonon according to the real and imaginary parts of the self-energy, respectively. Without explicit calculation, one can estimate the scale of the broadening as $\text{Im}[\Pi] \sim S^4 |\mathbb{A}|^2 D(\omega_0)$, where $S = 1/2$ is the spin quantum number, and $D(\omega_0)$ is the relevant density of states for spin excitations evaluated at the bare phonon frequency. We conclude that the scale of the computed couplings is compatible with the reported[109] anomalous broadening of the E_g^2 phonon on the scale of 0.3 - 0.4 meV. However, explicit calculations could confirm this in the future, as we have shown for MnPSe₃ in Ref. [69].

Regarding the \mathbf{G} and \mathbf{L} couplings, the spin operators

at $q = 0$ can take the form:

$$\mathbf{M} \equiv \mathbf{S}_{\text{Ru1}} + \mathbf{S}_{\text{Ru2}} \quad (58)$$

$$\mathbf{N} \equiv \mathbf{S}_{\text{Ru1}} - \mathbf{S}_{\text{Ru2}} \quad (59)$$

where \mathbf{M} corresponds to a uniform magnetization (a ferromagnetic order parameter), and \mathbf{N} corresponds to the antiferromagnetic Neel order parameter. M_c transforms as A_{2g} , while (M_a, M_{b^*}) transform as E_g . Similarly, N_c transforms as A_{2u} , while (N_a, N_{b^*}) transform as E_u . Then, the general forms of the \mathbf{G} couplings are:

$$A_{1g} : \mathbf{G}_{q=0}^{\text{Ru1}} = 0, \quad \mathbf{G}_{q=0}^{\text{Ru2}} = 0 \quad (60)$$

$$A_{2g} : \mathbf{G}_{q=0}^{\text{Ru1}} = \begin{pmatrix} A \\ A \\ A \end{pmatrix}, \quad \mathbf{G}_{q=0}^{\text{Ru2}} = \begin{pmatrix} A \\ A \\ A \end{pmatrix} \quad (61)$$

$$E_g : \mathbf{G}_{q=0}^{\text{Ru1}} = \begin{pmatrix} A+B \\ A-B \\ -2A \end{pmatrix}, \quad \mathbf{G}_{q=0}^{\text{Ru2}} = \begin{pmatrix} A+B \\ A-B \\ -2A \end{pmatrix} \quad (62)$$

$$A_{1u} : \mathbf{G}_{q=0}^{\text{Ru1}} = 0, \quad \mathbf{G}_{q=0}^{\text{Ru2}} = 0 \quad (63)$$

$$A_{2u} : \mathbf{G}_{q=0}^{\text{Ru1}} = \begin{pmatrix} A \\ A \\ A \end{pmatrix}, \quad \mathbf{G}_{q=0}^{\text{Ru2}} = \begin{pmatrix} -A \\ -A \\ -A \end{pmatrix} \quad (64)$$

$$E_u : \mathbf{G}_{q=0}^{\text{Ru1}} = \begin{pmatrix} A+B \\ A-B \\ -2A \end{pmatrix}, \quad \mathbf{G}_{q=0}^{\text{Ru2}} = \begin{pmatrix} -A-B \\ -A+B \\ 2A \end{pmatrix} \quad (65)$$

The A_{1g} and A_{1u} modes cannot couple directly to the spin via terms like $\mathbf{S} \cdot \mathbf{p}$. The A_{2g} mode can couple to the out-of-plane uniform magnetization. The A_{2u} mode can couple to the out-of-plane staggered magnetization. The E_g and E_u modes can couple to the in-plane uniform and staggered magnetizations, respectively. In table II, we show the computed \mathbf{G} for the $q = 0$ optical modes. It may be emphasized that these are all several orders of magnitude smaller than the computed \mathbf{A} couplings, as noted in the previous section.

The \mathbf{L} couplings follow similar symmetries as the \mathbf{G} couplings, except with consideration of the product of the representations $\Gamma(\nu) \otimes \Gamma(\nu')$. Given that the magnitude of \mathbf{L} is relatively small in the present case, it is most interesting to consider the effect on E_g and E_u modes, which would otherwise be degenerate in the absence of time-reversal symmetry breaking. For such modes, the \mathbf{L} interactions may lead to splitting of the phonons [67, 110]. Since $E_g \otimes E_g$ contains both A_{2g} and E_g , it is possible for all components of the uniform magnetization to couple to the E_g modes (see table III). Similarly, all components of the staggered magnetization can couple to the E_u modes at $q = 0$. However, it is only the out-of-plane component that is relevant for splitting of the E modes.

TABLE II. Computed \mathbf{G} couplings for the optical $q = 0$ modes. The parameters A and B refer to equations (60) - (65). For the E modes, we take the same linear combination as in Table I.

Label	Energy (meV)		$\mathbf{G}_{q=0,\nu}$ (10^{-3} meV)	
	Comp.	Exp.	A	B
E_g^{1a}			0	-1.34
E_g^{1b}	13.5	14.6[82]	0.77	0
A_{2u}^1	15.2	15.2[81]	0.42	
A_{2g}^1	15.8		-0.38	
E_g^{2a}			0	-10.7
E_g^{2b}	19.2	20.5[82]	6.16	0
E_u^{1a}			-5.75	0
E_u^{1b}	20.3	21.2[81]	0	-9.97
A_{1g}^1	23.7	27.5[82]	0	
E_g^{3a}	28.5	33.6[82]	0	-14.1
E_g^{3b}			-8.16	0
E_u^{2a}			5.10	0
E_u^{2b}	31.6		0	-8.82
A_{2g}^2	33.0		0.08	
E_g^{4a}			0	23.8
E_g^{4b}	33.6	36.8[82]	13.7	0
A_{2u}^2	33.6		0.03	
A_{1u}^1	36.8		0	
E_u^{3a}	37.4	~ 38 [81]	3.41	0
E_u^{3b}			0	-5.89
A_{1g}^2	37.6	37.5[82]	0	

TABLE III. Product table for D_{3d} .

	A_{1g}	A_{2g}	E_g	A_{1u}	A_{2u}	E_u
A_{1g}	A_{1g}	A_{2g}	E_g	A_{1u}	A_{2u}	E_u
A_{2g}		A_{1g}	E_g	A_{2u}	A_{1u}	E_u
E_g			$A_{1g} \oplus A_{2g} \oplus E_g$	E_u	E_u	$A_{1u} \oplus A_{2u} \oplus E_u$
A_{1u}				A_{1g}	A_{2g}	E_g
A_{2u}					A_{1g}	E_g
E_u						$A_{1g} \oplus A_{2g} \oplus E_g$

Specifying to $q = 0$, the Hamiltonian for the \mathbf{L} couplings reads:

$$\mathcal{H}_L = \frac{i}{2} \sum_{q\nu\nu'} (a_{0\nu}^\dagger a_{0\nu'}^\dagger + a_{0\nu} a_{0\nu'}) (\mathcal{L}_{(i)}^{0\nu;0\nu'} + \mathcal{L}_{(i)}^{0\nu';0\nu}) + (a_{0\nu}^\dagger a_{0\nu'} - a_{0\nu} a_{0\nu'}) (\mathcal{L}_{(i)}^{0\nu';0\nu} - \mathcal{L}_{(i)}^{0\nu;0\nu'}) \quad (66)$$

In practice, it is the latter term that is primarily responsible for splitting of the optical phonons in the presence of a finite magnetic order parameter. We find that this combination always transforms as A_{2g} , such that:

$$E_g, E_u : \frac{1}{2} (\mathbf{L}_{\text{Ru1}}^{0\nu;0\nu'} - \mathbf{L}_{\text{Ru1}}^{0\nu';0\nu}) = \begin{pmatrix} A \\ A \\ A \end{pmatrix} \quad (67)$$

$$\frac{1}{2} (\mathbf{L}_{\text{Ru2}}^{0\nu;0\nu'} - \mathbf{L}_{\text{Ru2}}^{0\nu';0\nu}) = \begin{pmatrix} A \\ A \\ A \end{pmatrix} \quad (68)$$

TABLE IV. Computed \mathbf{L} couplings for the optical $q = 0$ E modes. The parameter A refers to equations (67) - (68).

Label	Energy (meV)		A (10^{-3} meV)
	Comp.	Exp.	
E_g^1	13.5	14.6[82]	-17.9
E_g^2	19.2	20.5[82]	3.28
E_u^1	20.3	21.2[81]	10.2
E_g^3	28.5	33.6[82]	-21.6
E_u^2	31.6		9.18
E_g^4	33.6	36.8[82]	83.1
E_u^3	37.4	~ 38 [81]	0.85

Both the E_g and E_u modes couple to the out-of-plane uniform magnetization in this way. In table IV, we give the computed A parameters for each of the $q = 0$ optical E modes. The largest couplings are on the order of 0.08 meV, for the E_g^4 modes. It may be noted that a similar order of magnitude was recently computed [67, 68] for spin-phonon coupling-induced splitting of some of the E modes in the isostructural honeycomb material CrI_3 . However, a major difference is that $\alpha\text{-RuCl}_3$ orders as an antiferromagnet at zero field. Thus, a large out-of-plane field may be required to induce a sufficient uniform magnetization to observe such splitting.

S7. Effective Hamiltonian Formulation of Hall Viscosity

In this section, we provide an alternative derivation of the phonon Hall viscosity expression employed in Ref. 47 and 48. The goal is to derive an effective phonon Hamiltonian by integrating out the spins, given by:

$$\mathcal{H}_{\text{eff}} = - \lim_{i\omega_n \rightarrow i0} \frac{1}{2} \sum_{q\nu'\nu} (D_q^{\nu'\nu})^{-1} u_{-q\nu'} u_{q\nu} + (P_q^{\nu'\nu})^{-1} p_{-q\nu'} p_{q\nu} + (Q_q^{\nu'\nu})^{-1} p_{-q\nu'} u_{q\nu} + (W_q^{\nu'\nu})^{-1} u_{-q\nu'} p_{q\nu} \quad (69)$$

$$= - \lim_{i\omega_n \rightarrow i0} \frac{1}{2} \sum_q \mathbf{u}_q^\dagger \mathbf{D}_q^{-1} \mathbf{u}_q + \mathbf{p}_q^\dagger \mathbf{P}_q^{-1} \mathbf{p}_q + \mathbf{p}_q^\dagger \mathbf{Q}_q^{-1} \mathbf{u}_q + \mathbf{u}_q^\dagger \mathbf{W}_q^{-1} \mathbf{p}_q \quad (70)$$

with $\omega_n = 2n\pi/\beta$, $u_{q\nu} = (a_{-q\nu}^\dagger + a_{q\nu})$, and $p_{q\nu} = i(a_{-q\nu}^\dagger - a_{q\nu})$. Here, \mathbf{u}_q and \mathbf{p}_q are column vectors of phonon operators for different bands, and Greens function matrices have components $[\mathbf{D}_q]_{\nu,\nu'} = D_q^{\nu,\nu'}$. The limit is taken to mean $\lim_{i\omega_n \rightarrow i0} \equiv \frac{1}{2}(\lim_{i\omega_n \rightarrow i0^+} + \lim_{i\omega_n \rightarrow i0^-})$. This form ensures that (a) the limit is well-defined, and (b) the resulting Hamiltonian is Hermitian. D, P, Q , and W are imaginary time ordered Greens functions defined by:

$$D_q^{\nu'\nu}(i\omega_n) = \int_0^\beta d\tau e^{i\omega_n\tau} \langle \mathcal{T}_\tau u_{-q\nu'}(\tau) u_{q\nu}(0) \rangle \quad (71)$$

$$P_q^{\nu'\nu}(i\omega_n) = \int_0^\beta d\tau e^{i\omega_n\tau} \langle \mathcal{T}_\tau p_{-q\nu'}(\tau) p_{q\nu}(0) \rangle \quad (72)$$

$$Q_q^{\nu'\nu}(i\omega_n) = \int_0^\beta d\tau e^{i\omega_n\tau} \langle \mathcal{T}_\tau p_{-q\nu'}(\tau) u_{q\nu}(0) \rangle \quad (73)$$

$$W_q^{\nu'\nu}(i\omega_n) = \int_0^\beta d\tau e^{i\omega_n\tau} \langle \mathcal{T}_\tau u_{-q\nu'}(\tau) p_{q\nu}(0) \rangle \quad (74)$$

We consider a Hamiltonian given by $\mathcal{H} = \mathcal{H}_0 + \sum_{q\nu} \mathcal{A}_{q\nu} u_{q\nu}$, where $\mathcal{A}_{q\nu}$ is the spin-phonon coupling bond operator defined in the main text, and $\mathcal{H}_0 = \sum_{q\nu} \omega_{q\nu} (a_{q\nu}^\dagger a_{q\nu} + 1/2)$ is the bare phonon Hamiltonian. The zeroth order Greens functions are:

$$D_{0q}^{\nu'\nu}(i\omega_n) = \left(\frac{2\omega_{q\nu}}{(i\omega_n)^2 - \omega_{q\nu}^2} \right) \delta_{\nu,\nu'} \quad (75)$$

$$P_{0q}^{\nu'\nu}(i\omega_n) = D_{0q}^{\nu'\nu}(i\omega_n) \quad (76)$$

$$Q_{0q}^{\nu'\nu}(i\omega_n) = -i \left(\frac{2i\omega_n}{(i\omega_n)^2 - \omega_{q\nu}^2} \right) \delta_{\nu,\nu'} \quad (77)$$

$$W_{0q}^{\nu'\nu}(i\omega_n) = -Q_{0q}^{\nu'\nu}(i\omega_n) \quad (78)$$

We introduce the time ordered spin (bond-bond) correlation function:

$$A_{0q}^{\nu'\nu}(i\omega_n) = \int_0^\beta d\tau e^{i\omega_n\tau} \langle \mathcal{T}_\tau \mathcal{A}_{q\nu}(\tau) \mathcal{A}_{-q\nu'}(0) \rangle \quad (79)$$

Then, at one loop order, the Greens functions are given by the Dyson equations:

$$\mathbf{D}_q = (\mathbf{D}_{0q}^{-1} - \mathbf{A}_{0q})^{-1} \quad (80)$$

$$\mathbf{P}_q = \mathbf{D}_{0q} \quad (81)$$

$$\mathbf{Q}_q = (\mathbf{Q}_{0q}^{-1} - \mathbf{A}_{0q} \mathbf{D}_{0q} \mathbf{Q}_{0q}^{-1})^{-1} \quad (82)$$

$$\mathbf{W}_q = (\mathbf{W}_{0q}^{-1} - \mathbf{W}_{0q}^{-1} \mathbf{D}_{0q} \mathbf{A}_{0q})^{-1} \quad (83)$$

This leads to:

$$\begin{aligned} \mathcal{H}_{\text{eff}} = & - \lim_{i\omega_n \rightarrow i0} \frac{1}{2} \sum_q \mathbf{u}_{-q} (\mathbf{D}_{0q}^{-1} - \mathbf{A}_{0q}) \mathbf{u}_q + \mathbf{p}_{-q} \mathbf{P}_{0q}^{-1} \mathbf{p}_q \\ & + \mathbf{p}_{-q} (\mathbf{Q}_{0q}^{-1} - \mathbf{A}_{0q} \mathbf{D}_{0q} \mathbf{Q}_{0q}^{-1}) \mathbf{u}_q + \mathbf{u}_{-q} (\mathbf{W}_{0q}^{-1} - \mathbf{W}_{0q}^{-1} \mathbf{D}_{0q} \mathbf{A}_{0q}) \mathbf{p}_q \end{aligned} \quad (84)$$

Evaluating the limits gives:

$$\lim_{i\omega_n \rightarrow i0} \mathbf{D}_{0q}^{-1} = -\frac{1}{2} \Lambda_q \quad (85)$$

$$\lim_{i\omega_n \rightarrow i0} \mathbf{P}_{0q}^{-1} = -\frac{1}{2} \Lambda_q \quad (86)$$

$$\lim_{i\omega_n \rightarrow i0} \mathbf{Q}_{0q}^{-1} = 0 \quad (87)$$

$$\lim_{i\omega_n \rightarrow i0} \mathbf{W}_{0q}^{-1} = 0 \quad (88)$$

$$\lim_{i\omega_n \rightarrow i0} \mathbf{A}_{0q} \mathbf{D}_{0q} \mathbf{Q}_{0q}^{-1} = \lim_{i\omega_n \rightarrow i0} i \left(\frac{\Lambda_q}{i\omega_n} \right) \mathbf{A}_{0q} \quad (89)$$

$$\lim_{i\omega_n \rightarrow i0} \mathbf{W}_{0q}^{-1} \mathbf{D}_{0q} \mathbf{A}_{0q} = \lim_{i\omega_n \rightarrow i0} -i \mathbf{A}_{0q} \left(\frac{\Lambda_q}{i\omega_n} \right) \quad (90)$$

where Λ_q is a diagonal matrix of $\omega_{q\nu}$ values. This gives:

$$\mathcal{H}_{\text{eff}} = \frac{1}{4} \sum_q (\mathbf{u}_q^\dagger \Lambda_q \mathbf{u}_q + \mathbf{p}_q^\dagger \Lambda_q \mathbf{p}_q) - \lim_{i\omega_n \rightarrow i0} \frac{1}{2} \sum_q \mathbf{u}_q^\dagger \mathbf{A}_{0q} \mathbf{u}_q + \frac{i}{i\omega_n} (\mathbf{u}_q^\dagger \mathbf{A}_{0q} \Lambda_q \mathbf{p}_q - \mathbf{p}_q^\dagger \Lambda_q \mathbf{A}_{0q} \mathbf{u}_q) \quad (91)$$

$$= \mathcal{H}_0 - \lim_{i\omega_n \rightarrow i0} \frac{1}{2} \sum_q \mathbf{u}_q^\dagger \mathbf{A}_{0q} \mathbf{u}_q + \frac{i}{i\omega_n} (\mathbf{u}_q^\dagger \mathbf{A}_{0q} \Lambda_q \mathbf{p}_q - \mathbf{p}_q^\dagger \Lambda_q \mathbf{A}_{0q} \mathbf{u}_q) \quad (92)$$

The first term is simply the zeroth order phonon Hamiltonian. The rest of the expression is the zero frequency limit of the self-energy at one loop order. Taking the zero-temperature limit of the spin correlation function gives:

$$A_{0q}^{\nu\nu'}(i\omega_n) = \sum_{m \neq g} \frac{\langle g | \mathcal{A}_{q\nu} | m \rangle \langle m | \mathcal{A}_{-q\nu'} | g \rangle}{(E_m - E_g) - i\omega_n} + \frac{\langle g | \mathcal{A}_{-q\nu'} | m \rangle \langle m | \mathcal{A}_{q\nu} | g \rangle}{(E_m - E_g) + i\omega_n} \quad (93)$$

$$\approx \mathcal{P} \sum_{m \neq g} \frac{\langle g | \mathcal{A}_{q\nu} | m \rangle \langle m | \mathcal{A}_{-q\nu'} | g \rangle}{E_m - E_g} \left(1 + \frac{i\omega_n}{E_m - E_g} + \dots \right) + \frac{\langle g | \mathcal{A}_{-q\nu'} | m \rangle \langle m | \mathcal{A}_{q\nu} | g \rangle}{E_m - E_g} \left(1 - \frac{i\omega_n}{E_m - E_g} + \dots \right) \quad (94)$$

where $|g\rangle$ is the spin ground state and $|m\rangle$ is an excited spin state. Thus, we may evaluate the zero-frequency limits:

$$\lim_{i\omega_n \rightarrow i0} A_{0q}^{\nu\nu'}(i\omega_n) = \mathcal{P} \sum_{m \neq g} \frac{\langle g | \mathcal{A}_{q\nu} | m \rangle \langle m | \mathcal{A}_{-q\nu'} | g \rangle + \langle g | \mathcal{A}_{-q\nu'} | m \rangle \langle m | \mathcal{A}_{q\nu} | g \rangle}{E_m - E_g} \equiv 2[\mathbf{R}_q]_{\nu, \nu'} \quad (95)$$

$$\lim_{i\omega_n \rightarrow i0} \frac{i}{i\omega_n} A_{0q}^{\nu\nu'}(i\omega_n) = i\mathcal{P} \sum_{m \neq g} \frac{\langle g | \mathcal{A}_{q\nu} | m \rangle \langle m | \mathcal{A}_{-q\nu'} | g \rangle - \langle g | \mathcal{A}_{-q\nu'} | m \rangle \langle m | \mathcal{A}_{q\nu} | g \rangle}{(E_m - E_g)^2} \equiv 2[\mathbf{I}_q]_{\nu, \nu'} \quad (96)$$

so that finally:

$$\mathcal{H}_{\text{eff}} = \mathcal{H}_0 - \sum_q \mathbf{u}_q^\dagger \mathbf{R}_q \mathbf{u}_q + \mathbf{u}_q^\dagger (\mathbf{I}_q \Lambda_q) \mathbf{p}_q - \mathbf{p}_q^\dagger (\Lambda_q \mathbf{I}_q) \mathbf{u}_q \quad (97)$$

The term with \mathbf{R}_q is the zero-frequency limit of the real part of the phonon self-energy. The term with \mathbf{I}_q is the “scattering” contribution to the dissipationless phonon Hall viscosity analogous to the two-phonon “Raman” term discussed in various works [44–46].

Given that our notation deviates slightly from previous works, we present two equivalent approaches for evaluating the phonon Berry curvature from the above-defined quantities. The first approach follows the typical strategy employed for topological magnons [111, 112]. The phonon Hamiltonian can be written as a bosonic Bogoliubov-de Gennes Hamiltonian:

$$\mathcal{H}_{\text{eff}} = \frac{1}{2} \sum_q (\mathbf{a}_q^\dagger \ \mathbf{a}_{-q}) \mathcal{H}_q^a \begin{pmatrix} \mathbf{a}_q \\ \mathbf{a}_{-q}^\dagger \end{pmatrix} \quad (98)$$

$$\mathcal{H}_q^a = \begin{pmatrix} \Lambda_q - 2\mathbf{R}_q + 2i(\Lambda_q \mathbf{I}_q + \mathbf{I}_q \Lambda_q) & -2\mathbf{R}_q + 2i(\Lambda_q \mathbf{I}_q - \mathbf{I}_q \Lambda_q) \\ -2\mathbf{R}_q - 2i(\Lambda_q \mathbf{I}_q - \mathbf{I}_q \Lambda_q) & \Lambda_q - 2\mathbf{R}_q - 2i(\Lambda_q \mathbf{I}_q + \mathbf{I}_q \Lambda_q) \end{pmatrix} \quad (99)$$

where \mathbf{a}_q is a column vector of $a_{q\nu}$ operators for different phonon bands ν . Following [111–113], we then define a matrix \mathbf{g} , which is:

$$\mathbf{g} = \left[\begin{pmatrix} \mathbf{a}_q \\ \mathbf{a}_{-q}^\dagger \end{pmatrix}, (\mathbf{a}_q^\dagger \ \mathbf{a}_{-q}) \right] = \begin{pmatrix} \mathbb{I}_{N \times N} & 0 \\ 0 & -\mathbb{I}_{N \times N} \end{pmatrix} \quad (100)$$

where $\mathbb{I}_{N \times N}$ is the identity matrix of dimension N = the number of phonon bands. The phonon eigenvectors $\xi_{q\nu}^{La}$ and $\xi_{q\nu}^{Ra}$ are the left and right eigenvectors of $\mathbf{g}\mathcal{H}_q^a$ with eigenvalues $\lambda_{q\nu} \approx \pm\omega_{q\nu}$, and the 2D Berry curvature is given by:

$$\Omega_{q\nu}^{\text{BC}} = -\text{sign}(\lambda_{q\nu}) \text{Im} \left[\left(\frac{\partial}{\partial q_x} \xi_{q\nu}^{La} \right) \mathbf{g} \left(\frac{\partial}{\partial q_y} \xi_{q\nu}^{Ra} \right) - \left(\frac{\partial}{\partial q_y} \xi_{q\nu}^{La} \right) \mathbf{g} \left(\frac{\partial}{\partial q_x} \xi_{q\nu}^{Ra} \right) \right] \quad (101)$$

The second approach follows more closely the formulation in [46, 48]. We define $\psi_q = (\mathbf{u}_q, \mathbf{p}_q)^T$, and $\dot{\psi}_q = -i[\psi_q, \mathcal{H}_{\text{eff}}]$, and seek a Hamiltonian that satisfies $\dot{\psi}_q = -i\mathcal{H}_q^b \psi_q$. This is given by:

$$\mathcal{H}_q^b = i \begin{pmatrix} 4 \Lambda_q \mathbf{I}_q & \Lambda_q \\ -\Lambda_q + 4 \mathbf{R}_q & 4 \mathbf{I}_q \Lambda_q \end{pmatrix} \quad (102)$$

The phonon eigenvectors $\xi_{q\nu}^{Lb}$ and $\xi_{q\nu}^{Rb}$ are the left and right eigenvectors of \mathcal{H}_q^b with eigenvalues $\lambda_{q\nu} \approx \pm\omega_{q\nu}$. The Berry curvature may then be evaluated as:

$$\Omega_{q\nu}^{\text{BC}} = -\text{Im} \left[\left(\frac{\partial}{\partial q_x} \xi_{q\nu}^{L} \right) \left(\frac{\partial}{\partial q_y} \xi_{q\nu}^{R} \right) - \left(\frac{\partial}{\partial q_y} \xi_{q\nu}^{L} \right) \left(\frac{\partial}{\partial q_x} \xi_{q\nu}^{R} \right) \right] \quad (103)$$

The two approaches are ultimately equivalent. Finally, it may be noted that \mathcal{H}_q^b can be transformed to a form more familiar to [46, 48] by restoring the factors of $\sqrt{\omega_{q\nu}}$ appearing in the usual definition of the phonon operators. This is accomplished via a similarity transformation:

$$P = \begin{pmatrix} \Lambda_q^{1/2} & 0 \\ 0 & \Lambda_q^{-1/2} \end{pmatrix} \quad (104)$$

$$P^{-1} \mathcal{H}_q^b P = i \begin{pmatrix} 4 \Lambda_q^{1/2} \mathbf{I}_q \Lambda_q^{1/2} & \mathbb{I} \\ -\Lambda_q^2 + 4 \Lambda_q^{1/2} \mathbf{R}_q \Lambda_q^{1/2} & 4 \Lambda_q^{1/2} \mathbf{I}_q \Lambda_q^{1/2} \end{pmatrix} \quad (105)$$

In analogy with [48], we therefore identify the generalized phonon Hall viscosity $\eta_q^{\nu\nu'}$ (with units of energy/(r.l.u.)²) as:

$$|q|^2 \eta_q^{\nu\nu'} = 2 \left\langle \sum_{(i)} \mathcal{L}^{-q\nu; q\nu'} \right\rangle - 4 \left[\Lambda_q^{1/2} \mathbf{I}_q \Lambda_q^{1/2} \right]_{\nu\nu'} \quad (106)$$

$$= 2 \left\langle \sum_{(i)} \mathcal{L}^{-q\nu; q\nu'} \right\rangle + \lim_{i\omega_n \rightarrow i0} \frac{2i\sqrt{\omega_{q\nu}\omega_{q\nu'}}}{i\omega_n} \Pi_q^{\nu\nu'}(i\omega_n) \quad (107)$$

Here, we have reintroduced the \mathbf{L} couplings. As discussed above, $\mathcal{L} \propto |q|^2$. Since $\mathbf{I}_q \propto \mathcal{A}^2 \propto |q|$, the term $\Lambda_q^{1/2} \mathbf{I}_q \Lambda_q^{1/2} \propto |q|^2$, assuming linear dispersion of the acoustic phonons. As a consequence, the leading contribution to $\eta_q^{\nu\nu'}$ is momentum-independent.

S8. Evaluation of Thermal Conductivities and Intermediate Numerical Results

In this section, we discuss the expressions for the relative field-dependence of the phonon longitudinal thermal conductivity and thermal Hall conductivity employed in the main text. Following [53]:

$$\left. \frac{\kappa_{xy}^{2D}}{T} \right|_{\text{f.u.}} = -\frac{3}{2\pi^3} \sum_{\nu} \int_{\text{BZ}(2D)} d\vec{q} c_2 [n_{\text{B}}(\omega_{q\nu})] \Omega_{q\nu}^{\text{BC}} \quad (108)$$

where:

$$c_2(x) = (1+x) \left[\ln \left(\frac{1+x}{x} \right) \right]^2 - [\ln(x)]^2 - 2\text{Li}_2(-x) \quad (109)$$

$$n_{\text{B}}(E) = \frac{1}{e^{\frac{E}{k_{\text{B}}T}} - 1} \quad (110)$$

where f.u. indicates κ_{xy}/T is written in ‘‘fermionic units’’, i.e. as a multiple of the quantum of thermal conductivity $\pi k_{\text{B}}^2/(6\hbar)$. For low temperatures, the acoustic phonons at the edge of the Brillouin contribute little to the integral, because they are sufficiently high in energy. As such, the integral can be extended to infinite $|q|$, and written:

$$\left. \frac{\kappa_{xy}^{2D}}{T} \right|_{\text{f.u.}} \approx -\frac{3}{2\pi^3} \sum_{\nu} \int_0^{2\pi} \Omega_{\nu}^{\theta} d\theta \int_0^{\infty} |q|^2 c_2(f(c_{\nu}|q|)) d|q| \quad (111)$$

using $\Omega_{q\nu}^{\text{BC}} = \Omega_{\nu}^{\theta}|q|$ and $\omega_{q\nu} = c_{\nu}|q|$, where $c_{\nu} = \partial\omega_{q\nu}/\partial|q|$ is the speed of sound for each band, which we estimate as $c_{\text{ZA}} = 6.6$ meV/r1u, $c_{\text{TA}} = 11.7$ meV/r1u, and $c_{\text{LA}} = 28.2$ meV/r1u from the *ab-initio* phonon calculations. Introducing $x = \frac{c_{\nu}|q|}{k_{\text{B}}T}$ gives:

$$\left. \frac{\kappa_{xy}^{2D}}{T} \right|_{\text{f.u.}} \approx -\frac{3}{2\pi^3} \sum_{\nu} \left(\frac{k_{\text{B}}T}{c_{\nu}} \right)^3 \int_0^{2\pi} \Omega_{\nu}^{\theta} d\theta \int_0^{\infty} x^2 g(x) dx \quad (112)$$

$$\approx -2.00655 \sum_{\nu} \left(\frac{k_{\text{B}}T}{c_{\nu}} \right)^3 \int_0^{2\pi} \Omega_{\nu}^{\theta} d\theta \quad (113)$$

Thus, at fixed temperature,

$$\kappa_{xy}^{\text{ph}} \propto -\sum_{\nu} \left(\frac{1}{c_{\nu}} \right)^3 \int_0^{2\pi} d\theta \Omega_{\nu}^{\theta} \quad (114)$$

With similar considerations, the average in-plane longitudinal thermal conductivity follows:

$$\kappa_{xx}^{\text{ph}} \propto \sum_{\nu} \int_0^{2\pi} d\theta \int_0^{\infty} dx \frac{x^2 e^x}{(e^x - 1)^2} \tau_{\nu}^{\theta} \quad (115)$$

where:

$$\tau_{\nu}^{\theta} = \frac{\omega_{q\nu}}{\text{Im}[\Pi_{q\nu}(\omega_{q\nu})]} \quad (116)$$

is the momentum angle-dependent relative phonon lifetime. This leads to, at fixed temperature:

$$\kappa_{xx}^{\text{ph}} \propto \sum_{\nu} \int_0^{2\pi} d\theta \tau_{\nu}^{\theta} \quad (117)$$

We next discuss the details of numerical evaluation of κ_{xx} and κ_{xy} from the exact diagonalization (ED) bond correlations. In Fig. 7, we show the computed $\eta_q^{\nu\nu'}$. To obtain this, we take the discrete poles obtained from ED, and evaluate equation (96) without broadening. It may be noted that the off-shell approximation for the Hall viscosity has a pathological divergence when the spin-gap (quantified by $E_m - E_g$) becomes small, as would be expected near a critical point. When using the discrete poles from ED, this divergence is not problematic because the excitation gap

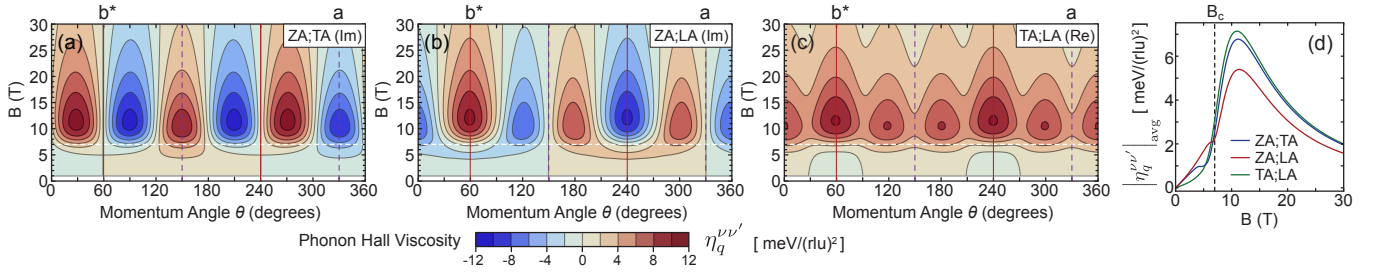


FIG. 7. Computed phonon Hall viscosity for $B \parallel a$, as a function of field and momentum angle θ . (a)-(c): $\eta_q^{\nu\nu'}(B)$ with $B_c = 7$ T indicated by a dashed white line. (d): Momentum-angle-integrated absolute value of $\eta_q^{\nu\nu'}(B)$. Calculations employed $(J, K, \Gamma, \Gamma', J_3) = (-2.79, -5.96, +3.06, -0.12, +0.8)$ meV and $g_{ab} = 2.3$.

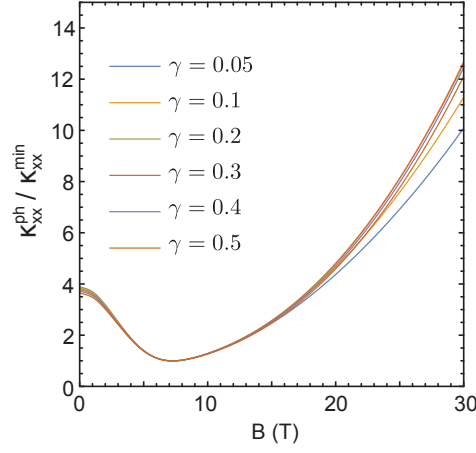


FIG. 8. Comparison of computed relative longitudinal phonon thermal conductivity as a function of Lorentzian broadening of the poles of the dynamical bond correlation functions obtained from exact diagonalization. Relative quantities such as $\kappa_{xx}^{\text{ph}}/\kappa_{xx}^{\text{min}}$ are insensitive to choice of broadening. $\gamma = 0.5$ meV is employed in the main text.

does not close at B_c due to finite size effects. A more complete quantitative treatment should go beyond the off-shell approximation to consider the full frequency dependence of the phonon self-energy.

It can be seen that the sign structure of $\eta_q^{\nu\nu'}$ changes substantially at the critical field B_c ; for many momentum directions, $\eta_q^{\nu\nu'}$ changes sign near B_c . Thus, despite the fact that spin-phonon scattering is generally enhanced near B_c , the peak in the Hall viscosity occurs at a field above the critical point. This leads to the maximum of κ_{xy}^{ph} also occurring above B_c , as discussed in the main text.

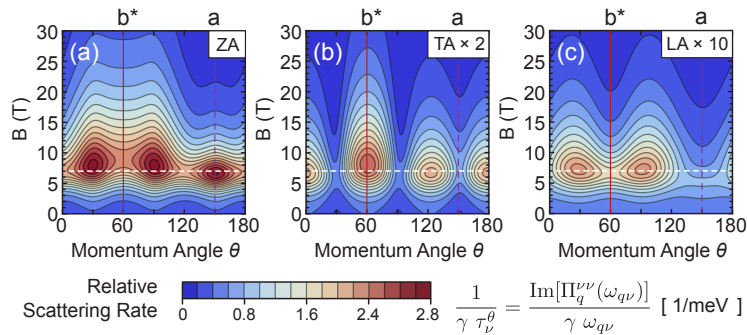


FIG. 9. Momentum angle dependence of the low-energy acoustic phonon scattering rate as a function of field $B \parallel a$, obtained for Lorentzian broadening $\gamma = 0.5$ meV. The critical field of the model $B_c = 7$ T is indicated by a horizontal dashed white line.

Finally, we comment on the numerical evaluation of $\text{Im}[\Pi_{q\nu}(\omega_{q\nu})]$. Since the discrete poles contributing to this function remain above 1 meV even at B_c due to finite size effects, it is necessary to extrapolate the dynamical bond correlations to lower frequency via broadening of the poles. As described in the main text, we choose a Lorentzian broadening $\delta(E - \omega) \rightarrow \frac{1}{\pi} \frac{\gamma}{(E - \omega)^2 + \gamma^2}$. This leads to an approximately linear dependence of the low-frequency $\text{Im}[\Pi_{q\nu}(\omega_{q\nu})]$ on γ . As a consequence, absolute magnitudes of the scattering rate cannot be resolved, but relative values remain robust. This is demonstrated in Fig. 8, where we plot $\kappa_{xx}^{\text{ph}}/\kappa_{xx}^{\text{min}}$ derived from different choices of broadening.

It may be of further interest to elaborate on the dependence of the scattering rate on in-plane propagation direction. At low frequency, $\text{Im}[\Pi_q^{\nu\nu}(\omega_{q\nu})] \propto \omega_{q\nu}$, such that $\tau_\nu^\theta = \omega_{q\nu}/\text{Im}[\Pi_q^{\nu\nu}(\omega_{q\nu})]$ has no explicit dependence on $|q|$. Thus, in Fig. 9 we show the evolution of the relative scattering rate $1/(\gamma \tau_\nu^\theta)$. Overall, this quantity shows a strong band- and θ -dependence, which stems from the variations in the form and magnitude of the spin-phonon couplings. The LA modes show, by far, the weakest spin-phonon scattering, and therefore dominate the longitudinal thermal transport. For $B \parallel a$, near the critical point, we predict $\kappa_{aa} > \kappa_{bb}$ as a result of the angular-dependence of the scattering rate.

S9. Phonon Hall Viscosity as an Electronic Berry Curvature

An interesting observation, highlighted in Ref. 67 and 68, is that the Hall viscosity can be interpreted in terms of a Berry phase acquired under adiabatic evolution of the atomic positions. To see this connection, we consider the instantaneous spin Hamiltonian to be $\mathcal{H}_{\text{sp}} = \mathcal{H}_s^0 + \sum_q \mathcal{A}_{q\nu}(u_{q\nu})$, where \mathcal{H}_s^0 is the bare magnetic interactions. Then it follows that:

$$\mathcal{A}_{q\nu} = \frac{\partial \mathcal{H}_{\text{sp}}}{\partial \langle u_{q\nu} \rangle} \quad (118)$$

Consider $|g\rangle$ to be the instantaneous ground state of \mathcal{H}_{sp} , such that:

$$\mathcal{H}_{\text{sp}}|g\rangle = E_g|g\rangle \quad (119)$$

Taking derivatives of both sides:

$$\frac{\partial}{\partial \langle u_{q\nu} \rangle} \mathcal{H}_{\text{sp}}|g\rangle = \frac{\partial}{\partial \langle u_{q\nu} \rangle} E_g|g\rangle \quad (120)$$

$$\frac{\partial \mathcal{H}_{\text{sp}}}{\partial \langle u_{q\nu} \rangle} |g\rangle + \mathcal{H}_{\text{sp}} \left| \frac{\partial g}{\partial \langle u_{q\nu} \rangle} \right\rangle = E_g \left| \frac{\partial g}{\partial \langle u_{q\nu} \rangle} \right\rangle \quad (121)$$

$$(E_g - \mathcal{H}_{\text{sp}})^{-1} \mathcal{A}_{q\nu} |g\rangle = \left| \frac{\partial g}{\partial \langle u_{q\nu} \rangle} \right\rangle \quad (122)$$

Thus, it follows that:

$$\frac{\langle m | \mathcal{A}_{q\nu} | g \rangle}{E_g - E_m} = \left\langle m \left| \frac{\partial g}{\partial \langle u_{q\nu} \rangle} \right\rangle \right\rangle \quad (123)$$

and therefore:

$$2[\mathbf{I}_q]_{\nu,\nu'} = i \left[\left\langle \frac{\partial g}{\partial \langle u_{q\nu} \rangle} \left| \frac{\partial g}{\partial \langle u_{-q\nu'} \rangle} \right\rangle \right\rangle - \left\langle \frac{\partial g}{\partial \langle u_{-q\nu'} \rangle} \left| \frac{\partial g}{\partial \langle u_{q\nu} \rangle} \right\rangle \right] \quad (124)$$

This expression is precisely the Berry curvature associated with the geometric phase that the spin wavefunction

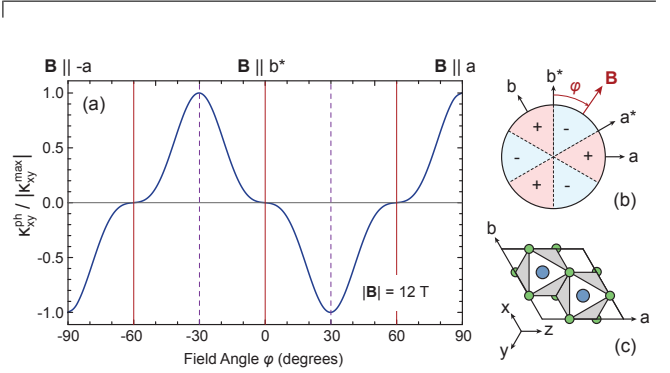


FIG. 10. (a) Field angle dependence of κ_{xy}^{ph} at $|\mathbf{B}| = 12$ T, for fields between $B \parallel -a$ and $B \parallel +a$. (b) Sign of κ_{xy} as a function of field direction, with definition of field angle ϕ . (c) Orientation of the unit cell and cubic x, y, z coordinates.

acquires under adiabatic evolution of the atomic positions (along the trajectories defined by the eigenvectors of the phonon bands ν and ν'). The \mathbf{L} couplings discussed in previous sections have a similar interpretation: these account for the contribution to the Berry phase due to evolution of the specific spin-orbital composition of the local moments, due to mixing with states outside of the low-energy spin basis. Thus \mathbf{L} and \mathbf{I} capture the same effect; the former is obtained by integrating out the higher energy electronic states, the latter is obtained by integrating out the low-energy spin degrees of freedom.

S10. Field-Angle Dependence of κ_{xy}

To investigate the dependence of κ_{xy}^{ph} on the direction of the in-plane field, we repeated the above-described calculations for $|\mathbf{B}| = 12$ T for a range of in-plane fields between $-a$ and $+a$. The results are shown in Fig. 10. It may be noted that the various experimental reports of κ_{xy} in α -RuCl₃ employ different coordinate systems, which should be considered when comparing different studies. The important consideration is the orientation of the cubic axes with respect to the crystallographic

axes. For example, Ref. [9] refers to a monoclinic cell, in which the crystallographic a -axis corresponds with the a -axis employed in our calculations. They report $\kappa_{xy} > 0$ for $B \parallel a$, which is consistent with our findings for the phononic contribution. In contrast, Ref. [3, 4] consider a monoclinic cell with $-a$ corresponding with our a -axis. Consistently, they report $\kappa_{xy} > 0$ for $B \parallel -a$ (in their coordinate definition), which also consistent with our findings and Ref. [9]. Overall, for in-plane fields, we find that $\text{sign}(\kappa_{xy}^{\text{ph}}) = \text{sign}(h_x h_y h_z)$, where h_x is the projection of the magnetic field on the cubic x -axis. This mimics the expected angle-dependence for the pure Kitaev spin-liquid. However, the experimentally observed sign-structure is also the simplest that is compatible with the symmetries of the crystal. For $B \parallel b^*$ or $B \parallel a^*$, we find that κ_{xy}^{ph} vanishes. This is enforced by C_2 symmetry in the polarized phase [27, 114], independent of the nature of the heat carrier. We also find that $|\kappa_{xy}^{\text{ph}}|$ is maximized for $B \parallel a$ and symmetry-related directions. We therefore conclude that the computed sign structure of κ_{xy}^{ph} matches the experimental field-angle dependence in the polarized phase.